EphrinA5 regulates cell motility by modulating *Snhg15*/DNA triplex-dependent targeting of DNMT1 to the *Ncam1* promoter

Can Bora Yildiz[1,2], Tathagata Kundu[3], Julia Gehrmann[4], Jannis Koesling[1], Amin Ravaei[1,5], Philip Wolff[1], Florian Kraft[6], Tiago Maié[4], Mira Jakovcevski[1], Daniel Pensold[1], Olav Zimmermann[3†], Giulia Rossetti[3,7,8†], Ivan G. Costa[4†] and Geraldine Zimmer-Bensch[1,2*†]

Abstract

Cell–cell communication is mediated by membrane receptors and their ligands, such as the Eph/ephrin system, orchestrating cell migration during development and in diverse cancer types. Epigenetic mechanisms are key for integrating external "signals", e.g., from neighboring cells, into the transcriptome in health and disease. Previously, we reported ephrinA5 to trigger transcriptional changes of lncRNAs and protein-coding genes in cerebellar granule cells, a cell model for medulloblastoma. LncRNAs represent important adaptors for epigenetic writers through which they regulate gene expression. Here, we investigate a lncRNA-mediated targeting of DNMT1 to specific gene loci by the combined power of in silico modeling of RNA/DNA interactions and wet lab approaches, in the context of the clinically relevant use case of ephrinA5-dependent regulation of cellular motility of cerebellar granule cells. We provide evidence that *Snhg15*, a cancer-related lncRNA, recruits DNMT1 to the *Ncam1* promoter through RNA/DNA triplex structure formation and the interaction with DNMT1. This mediates DNA methylation-dependent silencing of *Ncam1*, being abolished by ephrinA5 stimulation-triggered reduction of *Snhg15* expression. Hence, we here propose a triple helix recognition mechanism, underlying cell motility regulation via lncRNA-targeted DNA methylation in a clinically relevant context.

Keywords DNA methylation, Nuclear actions of Snhg15, Long non-coding RNA, RNA/DNA triple helix, Cell migration, Medulloblastoma

†Olav Zimmermann, Giulia Rossetti, Ivan G. Costa, and Geraldine Zimmer-Bensch contributed equally to this work.

*Correspondence:
Geraldine Zimmer-Bensch
zimmer_geraldine@yahoo.de; zimmer@bio2.rwth-aachen.de
Full list of author information is available at the end of the article

Yildiz *et al. Epigenetics & Chromatin*   (2023) 16:42

Page 2 of 19

Graphical Abstract
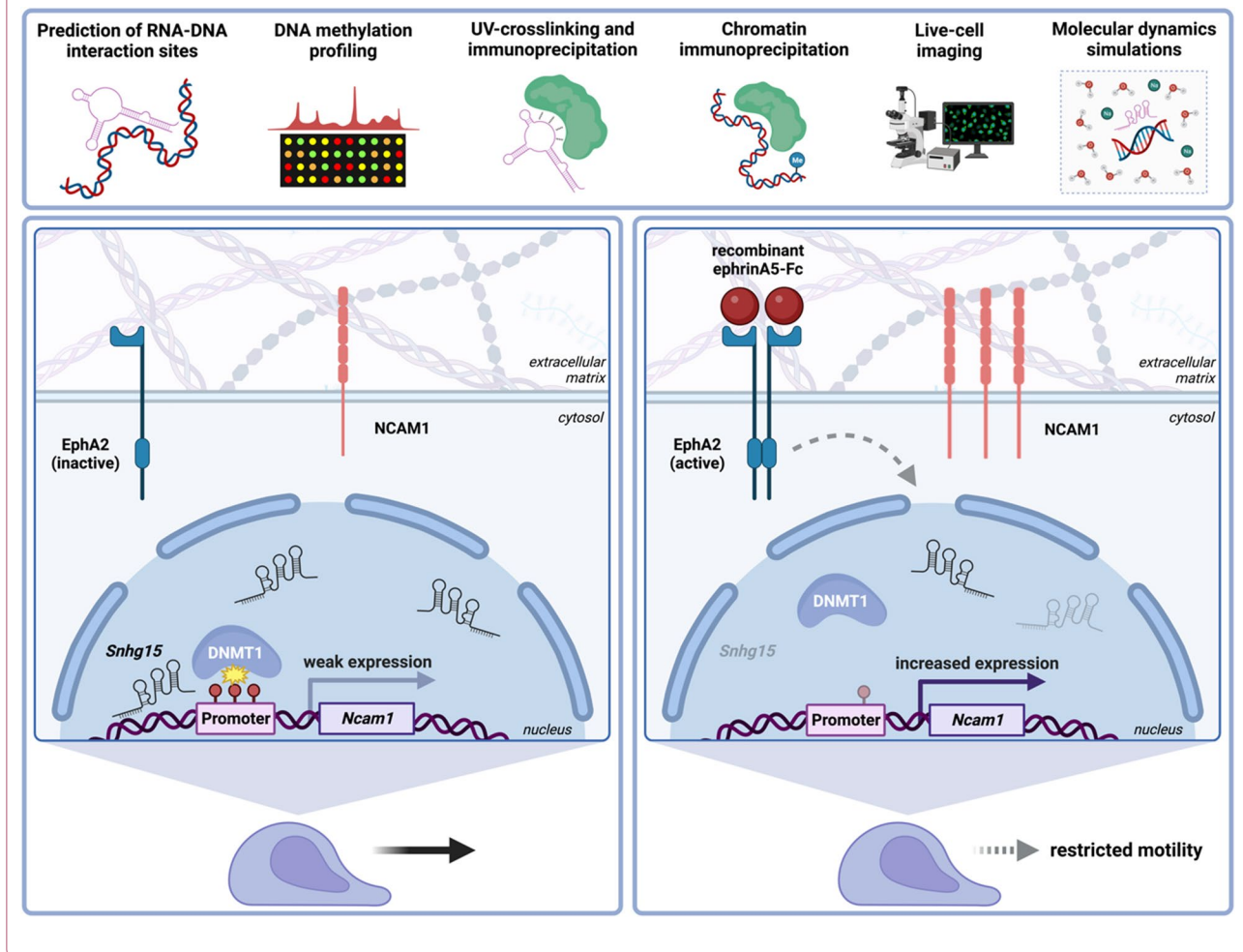
Introduction

Cells communicate with the local microenvironment. The perception of those external signals, provided, e.g., by the extracellular matrix (ECM) or cell surface molecules of neighboring cells, is critically involved in regulating cell intrinsic processes that orchestrate cellular proliferation, differentiation, and migration. Apart from proper morphogenesis of tissues and organs, these developmental processes play a key role in tumor initiation and/or progression [1–3].

The membrane-bound Eph receptors and their cognate ligands, the ephrins, represent signaling molecules that on the one hand orchestrate the development of various tissues including brain structures [4–8], and cancer-related aspects on the other hand. The Eph/ephrin system was found to be implicated in numerous types of brain cancer, such as glioblastoma and medulloblastoma [9–11]. Of note, the expression of ephrinA5 has been found dramatically downregulated in primary gliomas, and the forced expression of *EFNA5* (encoding for ephrinA5) diminishes the tumorigenicity of human glioma cells [12, 13]. EPHA2, an Eph receptor known to interact with ephrinA5, has been reported to have not only tumor suppressive but also pro-oncogenic functions [14–16].

Even though the physiological relevance of Eph/ephrin signaling has been well-proven for developmental and cancer-related processes, whether and how the ligand-mediated activation of Eph receptors triggers changes in gene expression that underlie discrete cell physiological responses is greatly unknown. Typically, transcriptional regulation is fine-tuned by epigenetic mechanisms, comprising histone modifications, DNA methylation, and non-coding RNAs (ncRNAs). Apart from functional

Yildiz *et al. Epigenetics & Chromatin*   (2023) 16:42

Page 3 of 19

implications in directing developmental processes, it is widely accepted that dysregulated epigenetic signatures are associated with the initiation and progression of cancer [17–20].

DNA methylation, carried out by DNA methyltransferases (DNMTs), is one of the most frequently investigated epigenetic mechanism [21–23]. An important DNA methyltransferase is DNMT1, relevant for de novo methylation activity in cancer cells and maintaining the methylation state during proliferation [24, 25]. Moreover, DNMT1 was shown to crosstalk with histone modifiers, such as histone deacetylases and histone methylases, to alter the accessibility of the DNA [26, 27]. The DNA methylation landscape has been shown to vary dynamically depending on the cell type and the developmental stage, and to respond to external signals [28–30]. DNMT1 function and DNA methylation regulate a broad spectrum of physiological processes, including the migration of neurons [31] and glioma cells [32, 33]. However, whether and how DNMT targets specific gene loci, and induces transcriptionally relevant changes in DNA methylation signatures that elicit physiological responses, is not fully understood. Specifically, to which extent this cascade can be triggered by external signals provided, for instance, by the Eph/ephrin system, remains elusive so far.

We recently provided evidence that the stimulation of cell culture models for medulloblastoma, namely immortalized cerebellar granule (CB) as well as DAOY cells, with ephrinA5, a known tumor suppressor in glioma, has the potential to alter the expression of protein-coding genes and lncRNAs, such as the cancer-relevant lncRNA *SNHG15* [34]. In addition to *SNHG15*, abnormal expression of diverse lncRNAs has been implicated in glioma and medulloblastoma molecular pathology [35, 36]. This suggests a functional relevance that needs to be better understood to leverage the potential of lncRNAs as putative therapeutic targets [37–39]. lncRNAs are known to regulate transcription through interacting with epigenetic writers or erasers [40–43]. By forming triplex structures [44–47], or during antisense transcription, lncRNAs can promote or prevent the binding of epigenetic modifiers to discrete genomic loci [40]. Here, we aim to test how ephrinA5-dependent signaling regulates gene expression, and cell physiological responses by lncRNA-mediated remodeling of epigenetic signatures.

Materials and methods

Cell culture
Cerebellar granule (CB) cells [48] were cultured as previously described [34]. Briefly, CB cells were incubated in Dulbecco's modified Eagle medium (DMEM) with high glucose (#11965084, Gibco), supplemented with 10% fetal bovine serum (FBS) (#S1810, Biowest), $1 \times$ GlutaMAX™ (#35050038, Thermo Scientific) and 24 mM KCl at 33 °C, and 5% CO_2 and 95% relative humidity. Upon thawing, the medium was additionally supplemented with 100 U/mL penicillin and 100 µg/mL streptomycin until the first passage.

Treatment with recombinant ephrinA5-Fc
Cells were stimulated with 5 µg/mL of either the recombinant ephrinA5-Fc (#374-EA, Biotechne) or Fc protein (#109–1103, Rockland) as control, both pre-clustered with 10 µg/mL Alexa488-conjugated anti-human IgG (#A11013, Invitrogen) for 30 min at RT.

Transfection of cells with siRNA oligos
24 h after seeding, cells were transfected with siRNA oligos targeting *Ncam1* (#sc-36017, SantaCruz Biotechnology) or *EphA2* (#sc-35320, SantaCruz Biotechnology) at a final concentration of 9 nM by forward lipofection using Lipofectamine 2000© (#11,668,019, Invitrogen) according to the manufacturer's protocol. A non-targeting Block-iT Alexa Fluor Red Fluorescent Control siRNA (#14,750,100, Invitrogen) was utilized as control.

Migration assay
Standard TC cell culture plates (#83.3922, Sarstedt) were coated with Geltrex™ (#A1413202, Gibco) at a final concentration of 0.2 mg/mL diluted in CB culture medium without phenol red. After a 60 min incubation at 33 °C, the excess medium was removed, and the cells were seeded at a density of 14 cells/mm^2 and incubated for 24 h prior to transfection with siRNA oligos. 24 h post transfection, the cells were stimulated with ephrinA5-Fc or control Fc as control as described in the previous section. After 24 h of ephrinA5-Fc or control Fc treatment, the cells were imaged for 24 h at 33 °C and 5% CO_2 using a Leica DMi8 inverted microscope equipped with the Thunder imaging platform. Images were taken every 20 min using a $10 \times$ objective and processed with Fiji (ImageJ). Following a minimum intensity *z*-stack projection, the background noise was reduced using the Basic default plugin, replacing the temporal mean. The corrected image stack was used to create a temporal color code for the first 20 h of imaging to demonstrate the different migration ranges. Next, the background was subtracted using the rolling ball algorithm, and the stack was de-speckled. After converting the stack to 8-bit, the contrast was enhanced, and the stack was binarized using the Yen algorithm. Subsequently, the binarized stack was despeckled again, and the inconsistencies were fixed using the option "Fill holes". The wrMTrck plugin was used, as previously described by Sharma et al. [49], to track cells with a migration time of at least 6 h. The plugin was run

Yildiz *et al. Epigenetics & Chromatin*   (2023) 16:42

Page 4 of 19

with the following parameters: minimum particle size at 180, maximum particle size at 2000, maximum particle velocity at 50, maximum area change at 400, minimum track length at 18, and fps at 0.0008. The fastest 50% fraction was used for further analyses.

Expression analysis via quantitative reverse transcription PCR (RT-qPCR)

Total RNA was purified with the TRIzol™ reagent (#15,596,018, Invitrogen) according to manufacturer's protocol. Subsequently, samples were treated with RNase-free DNase I (#EN0521, Thermo Scientific) according to manufacturer's instructions to eliminate possible genomic DNA contaminants. cDNA synthesis was performed by reverse transcription using the iScript cDNA Synthesis Kit (#1,708,890, Bio-Rad). Quantitative real-time PCR (qPCR) reactions were performed with 10 ng cDNA of each sample and the PowerUP SYBR Green qRT-PCR Kit (#A25741, Applied Biosystems) using the CFX96 thermocycler (Bio-Rad). Primer sequences are listed in Additional file 2: Table S1. Data analysis was performed via the previously described ΔΔCt method [50] using the reference gene *Atp5bp*. Normalized expression levels were calculated relative to control Fc-treated samples.

Chromatin immunoprecipitation (ChIP)

24 h following the ephrinA5-Fc or control Fc stimulation, 1.5×10^6 cells were lysed with digestion buffer (50 mM Tris–HCl pH 8.0, 1 mM $CaCl_2$, 0.2% (v/v) Triton X-100, 1% protease inhibitor cocktail (#I3786, Merck)). Chromatin was enzymatically sheared for 5 min at 37 °C with 0.2 mU/µL Micrococcal nuclease (MNase) (#N3755, Merck), and stopped with MNase stop buffer (110 mM Tris–HCl pH 8.0, 55 mM EDTA). After adding $2 \times$ RIPA buffer (280 mM NaCl, 1.8% (v/v) Triton X-100, 0.2% (v/v) SDS, 0.2% (v/v) sodium deoxycholate, 5 mM EGTA, and 1% protease inhibitor cocktail), the samples were centrifuged for 15 min at 4 °C and 21,130×g. Following the centrifugation, 1% (v/v) of the supernatant was used as input control, whereas 20% (v/v) was used for each immunoprecipitation (IP). The input control was incubated in TE buffer (10 mM Tris–HCl pH 8.0, 1 mM EDTA) supplemented with 40 mU/µL proteinase K (#P4850, Merck) for 2 h at 55 °C and 1200 rpm. Per IP, 25 µL of protein A-coupled Dynabeads (#10001D, Invitrogen) was prepared by washing them twice and resuspending to the original volume with $1 \times$ RIPA buffer (10 mM Tris–HCl pH 8.0, 1 mM EDTA, 140 mM NaCl, 1% (v/v) Triton X-100, 0.1% (v/v) sodium deoxycholate, 0.1% (v/v) SDS, and 0.1% protease inhibitor cocktail). Then, the IP samples were pre-cleaned with 10 µL of Dynabeads for 1 h at 4 °C with rotation. Following the

pre-clearing, the beads were discarded, and the IP samples were incubated overnight with 40 mg/mL rabbit anti-DNMT1 (1:25, #70,201, BioAcademia), mouse anti-H3K27me3 (1:25, #Ab6002, Abcam), or normal rabbit IgG (1:25, #12–370, Merck) antibody at 4 °C with rotation. After the overnight incubation, 10 µL of Dynabeads was added to the IP samples, followed by a 3 h incubation with rotation at 4 °C. Subsequently, the antibody-bound beads were washed five times with $1 \times$ RIPA buffer, once with LiCl wash buffer (250 mM LiCl, 10 mM Tris–HCl pH 8.0, 1 mM EDTA, 0.5% (v/v) Igepal CA-630, 0.5% (v/v) sodium deoxycholate, 0.1% protease inhibitor cocktail), and once with TE buffer. Following the final wash, the beads were re-suspended in TE buffer with 40 mU/µL proteinase K (#P4850, Merck) and incubated for 2 h at 55 °C and 1200 rpm. The DNA from the input control and IP samples was isolated using the ChIP DNA Clean and Concentrator Kit (#D5205, Zymo Research) according to manufacturer's guidelines. ChIP-qPCRs were performed using the isolated ChIP DNA and input control DNA as templates and the PowerUP SYBR Green qRT-PCR Kit (#A25741, Applied Biosystems) on the CFX96 thermocycler (Bio-Rad). The primer sequences are listed in Additional file 2: Table S1. Data analysis was performed by a double normalization, first against the input control to calculate recovery and then against IgG to calculate the fold enrichment.

UV-crosslinked immunoprecipitation (CLIP)

After 24 h of ephrinA5-Fc and control Fc treatment, cells were washed once with pre-warmed $1 \times$ Dulbecco's phosphate-buffered saline (DPBS) (#14190-094, Gibco). Next, 6 mL of ice-cold DEPC-treated PBS was applied to the cells which were subsequently irradiated with 150 mJ/cm² at 254 nm for 40 s, harvested with a cell scraper, gently homogenized, and transferred into microtubes. The cells were pelletized at 4 °C and 22,000×g for 30 s and lysed with the pre-cooled lysis buffer (50 mM Tris–HCl (pH 7.4), 100 mM NaCl, 1% (v/v) Tergitol, 0.1% (v/v) SDS, 0.5% (v/v) sodium deoxycholate) supplemented with 1% protease inhibitor cocktail, and 2% RiboLock RNase Inhibitor (#EO0381, Thermo Scientific). RNA was sheared, and the DNA was degraded for 3 min at 37 °C and 300 rpm using 45.8 mU/mL MNase (#N3755, Merck) and 36 U/mL DNase (#EN0521, Thermo Scientific). The reaction was stopped using the MNase stop buffer (110 mM Tris–HCl pH 8.0, 55 mM EDTA). The samples were centrifuged for 10 min at 4 °C and 22,000×g, and the supernatant was transferred into RNase-free microtubes. 1% (v/v) of the sample was isolated as input control, mixed with 500 µL TRIzol (#15,596,018, Invitrogen), snap-frozen on dry ice, and stored at -20℃

Yildiz *et al. Epigenetics & Chromatin*   (2023) 16:42

Page 5 of 19

until further use. Per immunoprecipitation, 25 mg/mL of rabbit anti-DNMT1 (1:40, #70,201, BioAcademia), rabbit anti-EZH2 (1:40, #5246S, Cell Signaling) or normal rabbit IgG (1:40, #12–370, Merck) antibody was pre-incubated with washed Dynabeads (#10001D, Invitrogen) for 1 h at RT to pre-coat the beads with antibodies. The IgG pulldown was applied to differentiate signal from noise due to unspecific binding of lncRNAs to rabbit epitopes [51]. 33% (v/v) of the sheared RNA samples were added to the different antibody–bead mixtures and rotated for 2 h at 4 °C to allow the antibodies to bind to their target protein. Next, the samples were washed twice with high salt buffer (50 mM Tris–HCl (pH 7.4), 1 M NaCl, 1 mM EDTA, 1% (v/v) Tergitol, 0.1% (v/v) SDS, 0.5% (v/v) sodium deoxycholate) followed by two washes with wash buffer (20 mM Tris–HCl (pH 7.4), 10 mM $MgCl_2$, 0.2% (v/v) Tween 20) at 4 °C, with each washing step lasting for 1 min with rotation. After discarding the supernatant, the beads were re-suspended in wash buffer supplemented with 20 mU/μL proteinase K (#P4850, Merck) and incubated with shaking for 20 min at 37 °C and 300 rpm. Afterward, the CLIP-RNA was purified alongside the input control with TRIzol™ reagent (#15,596,018, Invitrogen) according to manufacturer's protocol and used as template for the quantitative reverse transcription PCR. The CLIP-RT-qPCRs were performed using the SuperScript™ III Platinum™ SYBR™ Green One-Step kit (#11,736–051, Invitrogen) on the CFX96 thermocycler (Bio-Rad). The primer sequences are listed in the Additional file 2: Table S1. RNA recovery was calculated via normalization to the total amount of RNA per experiment and condition.

DNA methylation profiling

To achieve comparable results, we used cells obtained from the same passage as those used for RNA sequencing in Pensold et al. [34]. The cells were stimulated with ephrinA5-Fc or control Fc in parallel to the RNA sequencing experiments, harvested after 24 h, and stored at − 20 °C until the samples were further processed. The DNA was extracted using the PureLink® Genomic DNA Mini Kit (#K1820, Invitrogen). The samples were then treated with proteinase K and RNase A supplied in the kit. The DNA methylation profiling was carried out using the Infinium Mouse Methylation BeadChip (Illumina) according to the manufacturer's standard protocol. 500 ng of genomic DNA was bisulfite-converted using the Zymo EZ-96 DNA Methylation kit (Zymo Research, Irine, CA, USA). Subsequently, the bisulfite-converted DNA samples were amplified, fragmented, purified, and hybridized onto

the BeadChip array following the manufacturer's protocol. The arrays were washed and scanned using the Illumina iScan System. Mouse Methylation BeadChips were processed at Life & Brain (L&B) Genomics, Bonn.

Differential DNA methylation analysis

Differentially methylated regions/sites (DMRs/DMSs) were detected using the R packages Enmix [52], sva [53], and minfi [54]. The raw idat files were loaded by Enmix::readidat() together with Illumina's Infinium mouse-methylation manifest file (v.1.0). For background correction, dye bias correction, inter-array normalization, and probe type bias correction, we applied Enmix::mpreprocess() on the raw idat data setting the parameters qc and impute to TRUE. It returns a matrix of preprocessed methylation beta values. As a second preprocessing step, we used sva::ComBat() to mitigate the batch effect contained in these beta values which was introduced by different experiment runs under inevitably different conditions. The experiment run ID was set as the batch variable. Eventually, DMRs were identified by calling minfi::dmpFinder() on the preprocessed beta values. The parameter pheno was set to the respective cell conditions (for each sample either ctrl-Fc or efnA5-Fc) and the parameter type to="categorical". CpGs for which the dmpFinder result indicates a *p* value of 0.05 or smaller were considered significant DMRs. If not indicated otherwise, default parameters have been passed to the applied R functions.

We have compared the localization of DMSs on either hyper- or hypo-methylation regions to the location of all DMSs in the array (background) using the annotation provided by Illumina (shores, shelves, islands, intergenic). We used the binomial test to test if the number of DMSs in a region is higher than in the background. Due to the association with genes, we further annotated these DMSs to distinct locations (introns, exons, promoter, 5' and 3') using the "TxDb.Mmusculus.UCSC.mm10.knownGene" R package as reference. The cross between the annotations was done using the "annotatr" R package. Probes that were not annotated as CpGs were not considered for this analysis.

In silico *simulation of RNA/DNA interactions*

For *Adamts14*, the sequence-based predictions (method described in Pensold et al. [34]; sequences presented in Additional file 3: Table S2) suggested two slightly different alternatives for the 15-nucleotide binding mode, which were used to generate the two models, *Adamts14*-1 and *Adamts14*-2. For *Ncam1*, a 15-nucleotide sequence (*Ncam1*) as well as an extended sequence (*Ncam1*-ext) with additional base pairs (see Additional file 3: Table S2) was chosen. The latter was

introduced, as our preliminary evaluation revealed the binding site boundaries to be too narrow in this case and to cause artefactual strand separation. The extended version allowed us to evaluate the impact of termini fluctuations on the stability of the system in the simulations. To maintain comparability, we only evaluated sections that are also present in the non-extended *Ncam1* model.

All molecular dynamics simulations were carried out with the GROMACS simulation package (version 2021.4) using the AMBER-parmBSC1 force field [55] and TIP4P-D water model [56] in a rhombic dodecahedral box with periodic boundaries under standard conditions (300 K, 1 bar). We parameterized a protonated cytosine and used it for all cytosines that were not terminal. Potassium chloride, sodium chloride, and magnesium ions were added to the system. For the ions, the Joung and Cheatham parameters [57] were used. The concentrations are tuned to mimic the cellular environment with a sodium chloride concentration of 0.01 M and potassium chloride concentration of 0.1 M while magnesium ions were introduced to neutralize the total charge of the system. All ions were placed randomly in the simulation box.

To prepare for the simulation, each system underwent the following procedure: The potential energy of the system was minimized to eliminate clashes and bad contacts using the steepest descent energy minimization followed by conjugate gradient as implemented in GROMACS [58]. The initial minimization was followed by three preparatory steps: First, the system was heated up to 300 K by gradually increasing the temperature of the system from 0 to 300 K in 10 steps, lasting 1 ns each, using a Berendsen thermostat. Next, a simulation using an NVT (constant number, volume, and temperature) ensemble was conducted for 10 ns using position restraints with a force constant of 1000 kJ/(mol*nm^2) applied to all heavy atoms. Finally, a simulation in an NPT (constant number, pressure, and temperature) ensemble was conducted at 1 bar and 300 K for 10 ns. Velocity rescaling was used for temperature coupling with a time constant of 0.1 ps in order to ensure correct temperature fluctuations. For simulations at constant pressure, we used the Parrinello–Rahman pressure coupling algorithm [59] with a time constant of 2 ps. Afterward, at least 600 ns was simulated under NPT ensemble conditions with an integration step of 2 fs. All bonds were constrained using the LINCS algorithm [60]. A cutoff of 10 Å was used for Lennard–Jones and short-range Coulombic interactions and the particle mesh Ewald (PME) method was used for long-range electrostatic interactions with a grid spacing of 0.16 nm and an interpolation order of 4. The short-range Lennard–Jones interactions were handled using the grid system for neighbor searching. The cut-off distance for the neighbor list was 1.2 nm.

For visualization of the trajectory, we used VMD 1.9.3. For the analysis, we used VMD, tools provided by GROMACS, and our own scripts. Before analyzing the geometric properties of the trajectory, we eliminated periodic jumps and centered the solute using gmx trajconv.

Results

Snhg15 interaction with DNMT1 is diminished upon ephrinA5-Fc stimulation

We demonstrated earlier that ephrinA5-Fc stimulation of CB cells modulates the expression of protein-coding genes as well as of non-coding RNAs, including the cancer-associated lncRNA *Snhg15* [34]. Its human ortholog *SNHG15* has cancer- and metastasis-promoting functions, linked to poor survival in numerous human malignancies [61]. In addition to its well-documented action as a competitively endogenous RNA (ceRNA) sponging miRNAs in human cancers [62], *SNHG15* was reported to act in the nucleus in concert with EZH2 (Enhancer of zeste homolog 2), which is known to catalyze repressive trimethylation at histone 3 (H3K27me3) [63]. We found the expression of *Snhg15* to be reduced upon ephrinA5-Fc stimulation in CB and DAOY cells [34]. Using computational approaches, we predicted *Snhg15* to interact with the promoters of 19 protein-coding genes that were increased in expression upon ephrinA5-Fc stimulation [34]. These interactions were presumed to be driven by a predicted DNA-binding domain (DBD) in *Snhg15*, localized in nucleotide (nt) positions 1896–1925 [34]. Here, we asked whether these ephrinA5-triggered transcriptional changes of protein-coding genes are facilitated through *Snhg15*-mediated actions. Such actions could involve alterations of repressive epigenetic marks since lncRNAs were reported to recruit or to interact with epigenetic writers including DNMTs, and *SNHG15* in particular was described to interact with EZH2 in pancreatic cancer [63–66].

First, we verified whether *Snhg15* indeed interacts with epigenetic writers of repressive chromatin states, and whether this interaction is changed upon ephrinA5-Fc stimulation. To this end, we performed UV-mediated crosslinking of RNA with proteins in CB cells, followed by the immunoprecipitation of the protein of interest (CLIP). We chose to profile putative interactions of *Snhg15* with two major repressive epigenetic writers: EZH2, as the main enzyme of the PRC2 (Polycomb repressive complex 2) that catalyzes repressive trimethylations at H3K27 residues [67–69] and was described to act in concert with *Snhg15* [63], as well as DNMT1, one of the main DNA methyltransferases which catalyzes DNA

methylation triggering repressive states [21–23, 70]. Both proteins have been frequently implicated in transcriptional dysregulation which is a hallmark of glioma and medulloblastoma pathogenesis [71–77]. To investigate the potential interaction of EZH2 and/or DNMT1 with *Snhg15*, we performed antibody-mediated pulldown of EZH2- and DNMT1-bound RNA using CLIP. The specificity of the applied antibodies is shown in Additional file 1: Figure S1. Three different primer pairs covering distinct positions and isoforms of *Snhg15* (Fig. 1a, Additional file 1: Figure S2) were used for RT-qPCR-based analysis of the co-immuno-precipitated RNA. From the four known murine isoforms, only two isoforms (isoform

202 and 203) display the predicted DNA-binding domain (Fig. 1a). Both were covered by primer pair *SP1*. Primer pair *SP2* is specific for isoform 202, while primer pair *SP3* only detects isoform 203 (Fig. 1a).

CLIP experiments using the EZH2 antibody did not yield an RNA recovery above background noise, neither for control conditions (control Fc-treated cells) nor for the samples treated with ephrinA5-Fc (Additional file 1: Figure S2). In contrast, pulldown using a DNMT1-specific antibody resulted in a significant RNA recovery compared to IgG pulldown experiments at all tested loci (Fig. 1a and b), indicative of DNMT1 binding to *Snhg15*. Interestingly, ephrinA5-Fc treatment significantly
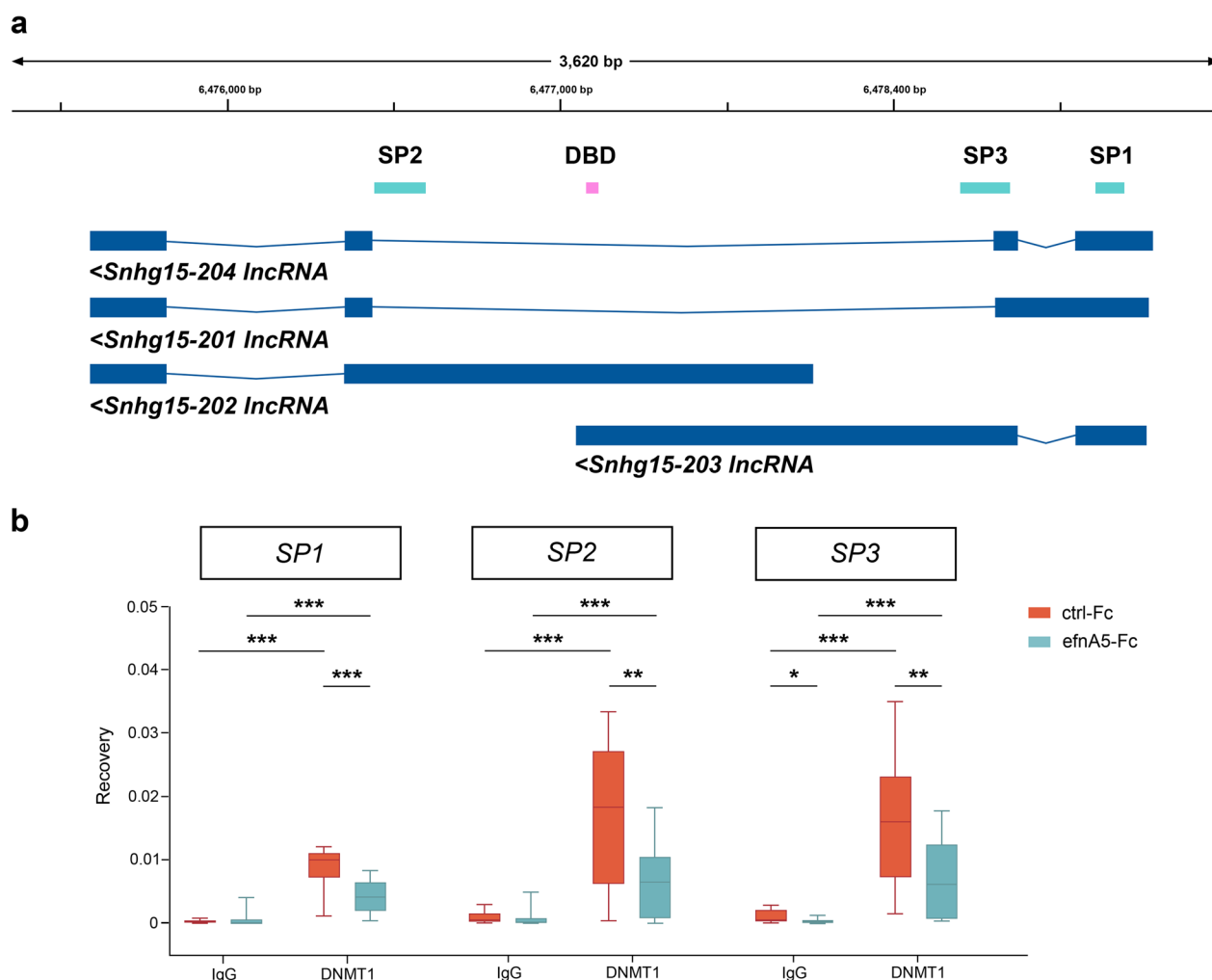
Fig. 1 *Snhg15* is associated with DNMT1 in an ephrinA5-dependent manner in CB cells. **a** Location of the three *Snhg15* amplicons used to amplify CLIP-RNA (from left to right: *SP2, SP3, SP1*) and the DNA-binding domain (DBD) location. **b** RNA recovery for IgG and anti-DNMT1 antibody CLIP samples in CB cells (N = 5 biological replicates). For amplicon positions *SP1, SP2,* and *SP3*, CLIP clearly indicated a (functional) association of DNMT1 with *Snhg15*, and a reduction of the amount of bound *Snhg15* RNA after ephrinA5-Fc stimulation. Whiskers of the box plots extend to the minimum and the maximum of the data values from the 25th and 75th percentiles (Spear style). Significances were determined with two-tailed Student's *t*-test. Significance levels: *p* value < 0.05 *; *p* value < 0.01 **; *p* value < 0.001 ***. ctrl-Fc: control Fc, efnA5-Fc: ephrinA5-Fc, CLIP: UV cross-linking and immunoprecipitation

Yildiz *et al. Epigenetics & Chromatin*   (2023) 16:42

Page 8 of 19

reduced the relative amount of DNMT1 association to *Snhg15* fragments at the tested loci (Fig. 1b). Together, these data propose that *Snhg15* directly interacts with DNMT1, and that this interaction is diminished by ephrinA5 stimulation.

EphrinA5-Fc stimulation impacts DNA methylation at promoters of *Snhg15* target genes such as *Ncam1*

DNMT1 catalyzes DNA methylation, which is often associated with gene repression [21, 22, 70, 78]. Thus, we next aimed to analyze, whether ephrinA5-Fc stimulation of CB cells induces changes in DNA methylation. To this end, DNA samples from CB cells treated with ephrinA5-Fc and control Fc were analyzed for changes in

CpG methylation using the Infinium Mouse Methylation BeadChip array.

The probes of the Infinium Mouse Methylation BeadChip array cover CpG shores, shelves, islands, and intergenic CpG sites (Fig. 2a). In response to ephrinA5-Fc stimulation, 6821 CpGs displayed a significant increase in DNA methylation levels, while 6392 CpGs were significantly reduced. We then analyzed the association of differentially methylated sites (DMSs) with distinct genetic elements. Thereby we have found DMSs in response to ephrinA5-Fc stimulation to be enriched in promoters, introns and in 1–5 kb region upstream of transcriptional start sites (TSS) (Fig. 2b). We detected numerous genes with decreased and increased CpG levels (Fig. 2c, Additional file 4: Table S3). These changes in DNA
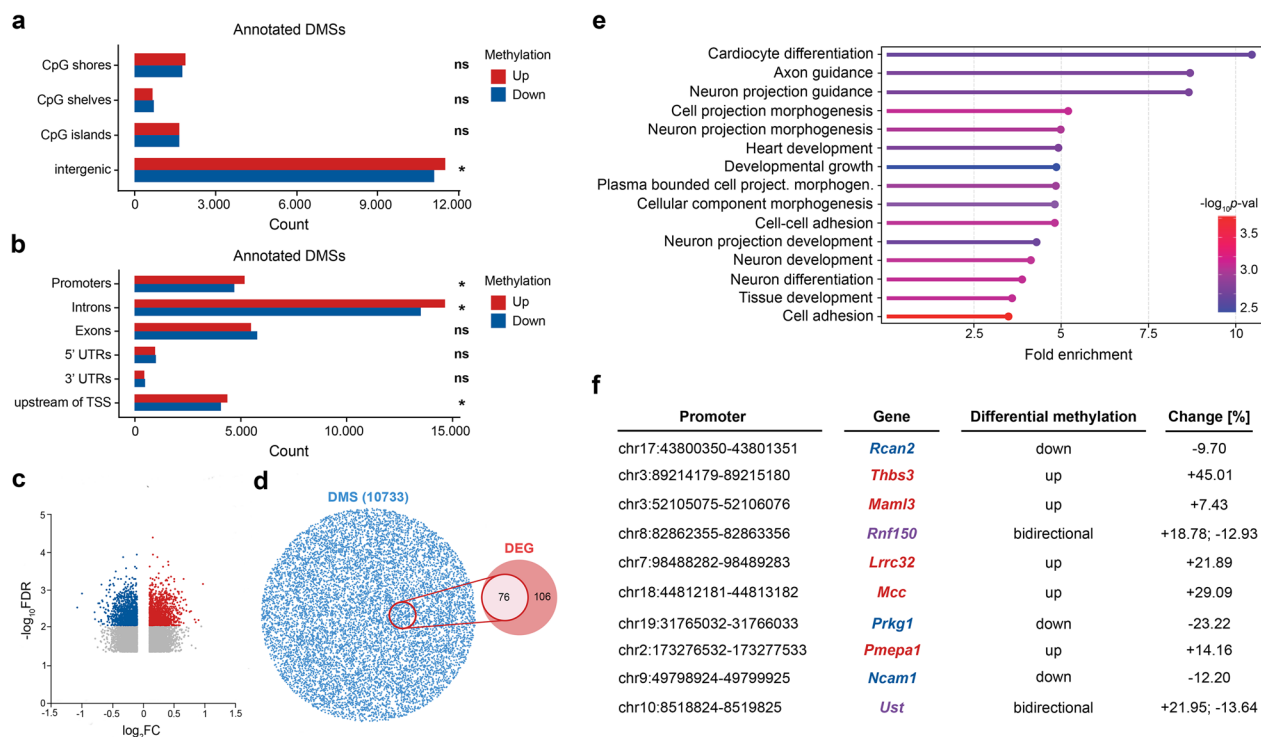
Fig. 2 EphrinA5-Fc stimulation induces changes in DNA methylation signatures, including cell adhesion-related genes. **a** Bar plot shows the localization of the differentially methylated CpG sites (DMS) in response to ephrinA5-Fc versus Fc stimulation detected with the Infinium Mouse Methylation BeadChip array across CpG shores, shelves, islands, and intergenic CpG sites. **b** A separation of DMSs based on their distribution across distinct genetic elements reveals them to be enriched in promoters, introns, and the 1–5 kb region upstream of the TSS. DMSs with upregulated methylation levels 24 h after ephrinA5-Fc are depicted in red while those with downregulated methylation levels are depicted in blue. **c** Volcano plot displays loci with significantly increased and decreased levels of DNA methylation, shown in red or blue, respectively, while differences below -$\log_{10}$p-val after false discovery rate (FDR) correction are depicted in gray. Loci changed below 0.1 $\log_2$FC (fold change) are excluded from the plot. **d** Venn diagram shows overlap between differentially expressed genes (DEG) and DMSs in ephrinA5-Fc-treated versus control-Fc-treated CB cells. **e** Gene Ontology analysis (GO) reveals enrichment for several GO terms related to cell adhesion and neuronal development; fold enrichment represented by the x-axis and -$\log_{10}$p-val is encoded by the color gradient. **f** Table lists all protein-coding genes with predicted binding sites for *Snhg15* that are upregulated (RNA-seq; Pensold et al. [34]) and simultaneously display DNA methylation changes 24 h after ephrinA5-Fc treatment. Genes with reduced methylation at discrete CpG sites are presented in blue font, red font indicates increased methylation at discrete CpG sites after ephrinA5-Fc treatment, while for genes with purple font CpG sites with increased as well as decreased methylation levels were detected. CB: cerebellar granule. TSS: transcription start site. UTR: untranslated region

methylation could explain the transcriptional changes observed earlier after ephrinA5-Fc treatment [34].

In support of these findings, about 42% of the differentially expressed genes displayed concomitant changes in DNA methylation (Fig. 2d). Among these genes that were both changed in transcription and in CpG methylation after ephrinA5-Fc stimulation, we determined a significant enrichment of cell adhesion-related genes by Gene Ontology (GO) analysis (Fig. 2e).

When focusing on the 19 genes upregulated after ephrinA5-Fc treatment and predicted to be bound by *Snhg15* via triple helix-mediated RNA–DNA interaction (Additional file 5: Table S4; Pensold et al. [34]), 10 of these genes showed significant alterations in the methylation of CpG sites, mostly close to the TSS (Fig. 2f, Additional file 4: Table S3). Methylation at the TSSs is usually associated with transcriptional repression [79]. According to our hypothesis, *Snhg15* interacts with DNMT1 as a repressive epigenetic writer, thereby recruiting DNMT1 to discrete gene loci, e.g., transcription start sites, and in concert leads to gene repression. Since the interaction of *Snhg15* and DNMT1 was diminished by ephrinA5-Fc stimulation, we were screening for genes with reduced CpG methylation close to their TSS among the 10 remaining genes (Fig. 2f). For *Rcan2*, *Prkg1*, and *Ncam1*, we detected an ephrinA5-Fc treatment-induced decrease in CpG methylation levels close to TSSs. Of note, *Ncam1* encodes the well-known adhesion protein NCAM1 (neural cell adhesion molecule 1), a crucial key player in not only neuronal but also cancer cell migration [80]. For various cancer types, elevated expression of *Ncam1*/*NCAM1*, like we observed after ephrinA5-Fc stimulation, is associated with reduced tumor cell migration and better prognosis [81, 82]. In line with this, we detected in patient data that increased expression levels of *NCAM1* in low-grade glioma are associated with improved survival rates (Additional file 1: Figure S3a).

Increased *Ncam1* expression level contributes to the ephrinA5-Fc triggered decrease in CB cell motility

In agreement with the inverse correlation of *NCAM1* expression with tumor cell migration [81, 82], we found reduced motility of CB cells, when analyzing their migration in vitro 24 h after ephrinA5-Fc stimulation (Fig. 3a and b). This time point was chosen since the elevated expression and diminished promoter methylation of *Ncam1* were detected here (Fig. 2d). Next, we aimed to verify, whether the ephrinA5-Fc-induced increase in *Ncam1* transcript levels accounts for the motility changes of CB cells. To this end, we performed live cell imaging experiments of cells 24 h after ephrinA5-Fc or control Fc stimulation, with a preceding siRNA-mediated knockdown of *Ncam1* (see Additional file 1: Figure S3b

for validation of knockdown efficiency). Indeed, the ephrinA5-Fc stimulation-triggered reduction of the migratory speed as well as the migration distance of CB cells compared to control Fc conditions was rescued by *Ncam1* siRNA application (Fig. 3a and b, Additional file 1: Fig. 3c). Of note, ephrinA5 is known to bind EphA2previously demonstrated to be highly expressed in CB cells [34]. To test, whether the ephrinA5-Fc triggered effect on cell motility in CB cells was dependent on EphA2, we knocked down the *EphA2* expression with target-specific siRNA oligos prior to ephrinA5-Fc or control Fc stimulation of cells (knockdown efficiency for the EphA2 is depicted in Additional file 1: Figure S4c). As a matter of fact, we found the motility-reducing effect of ephrinA5-Fc stimulation to be reversed to control levels after siRNA-mediated knockdown of *EphA2* (Additional file 1: Figure S4a and b). Together, these data propose that the ephrinA5-Fc triggered rise in *Ncam1* expression accounts for the impaired motility of CB cells, and that this mechanism is mediated by the EphA2 receptor.

Ncam1 is a potential target for *Snhg15*-mediated recruitment of DNMT1 and DNMT1-dependent DNA methylation

As we found decreased DNA methylation levels close to the TSS of *Ncam1* after ephrinA5-Fc stimulation of CB cells (Figs. 2d, 3c), we next aimed to elucidate whether DNMT1 binds to the *Ncam1* locus in an ephrinA5-Fc stimulation-dependent manner. Of note, in this current study, we have shown that ephrinA5-Fc treatment diminishes the interactions of DNMT1 with *Snhg15* (Fig. 1a and b). Hence, we next performed native chromatin immunoprecipitation (ChIP) in CB cells treated with ephrinA5-Fc and control Fc for 24 h prior to sample collection. A target-specific antibody was applied to pull down DNMT1 (verification of antibody specificity for DNMT1 is shown in Additional file 1: Figure S1a), and qPCR was performed to quantitatively assess the co-immuno-precipitated DNA fragments. To detect enrichment in the *Ncam1* locus, we used primer pairs targeting regions downstream (*P1* and *P2*) and upstream of the promoter (*P3* and *P4*). For regions covered by *P1* and *P2*, we did not detect any significant changes in the enrichment with DNMT1 upon stimulation with ephrinA5-Fc (Fig. 3c-e). The region covered by primer pair *P3*, in proximity to a candidate *cis*-regulatory element and surrounded by putative *Snhg15*-binding sites, presented a diminished association with DNMT1 after ephrinA5-Fc stimulation (Fig. 3f). In comparison, the primer pair *P4*, targeting a region upstream of putative *Snhg15*-binding sites, did not show altered DNMT1 enrichment after the stimulation (Additional file 1: Figure S5d). In contrast to the results for *Ncam1*, for *Adamts14*, no significant
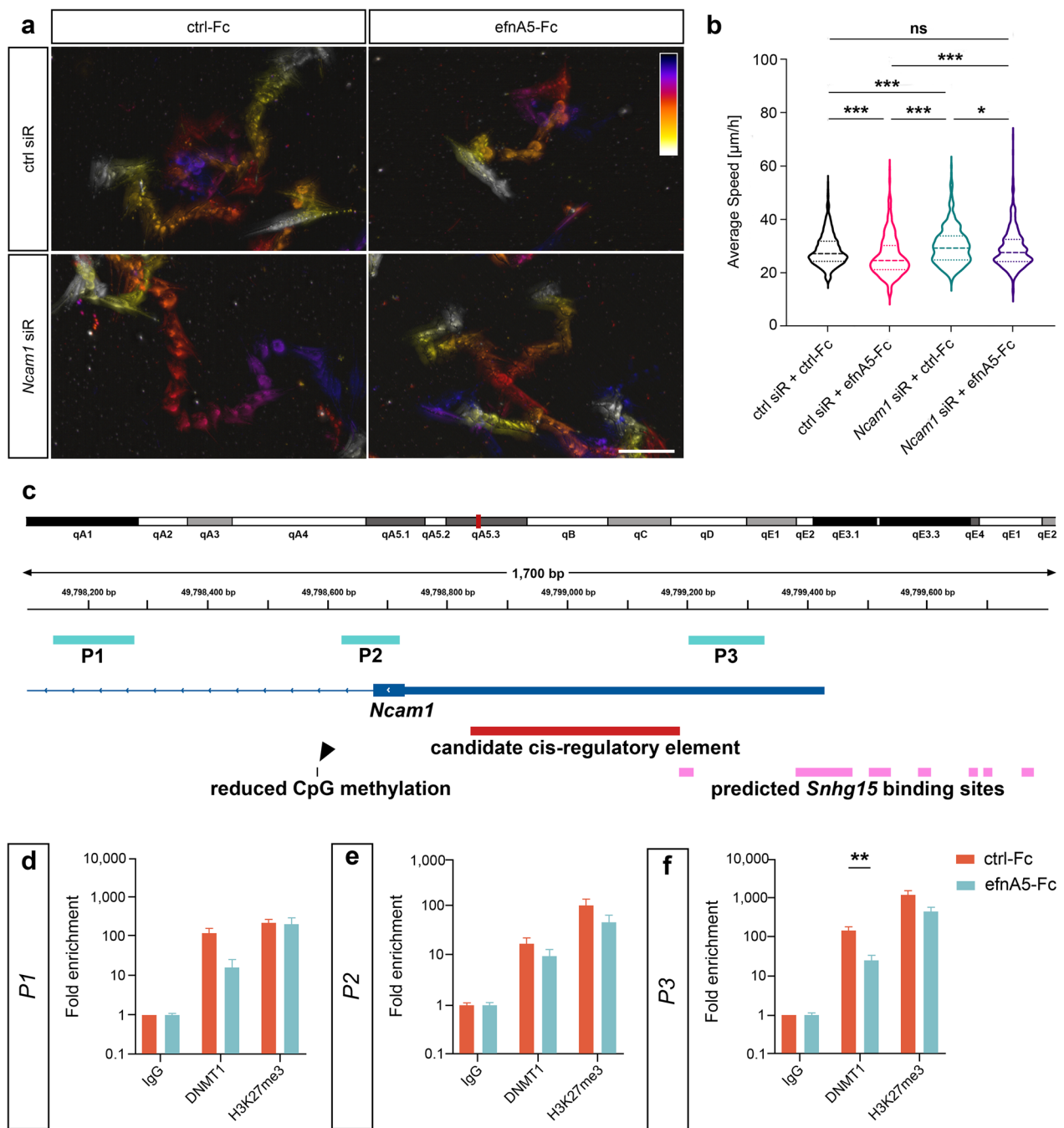
Fig. 3 EphrinA5 stimulation leads to reduced association of DNMT1 to *Ncam1* and diminished motility of CB cells. **a**, **b** The motility of CB cells is significantly reduced upon stimulation with ephrinA5-Fc, which can be rescued by a preceding knockdown of *Ncam1*. **a** Temporal color-coded migratory distance over 20 h of imaging. The starting point of migration for each cell is shown in dark blue and the end point in white. **b** Quantitative analysis of average migratory speed (n = 557 for ctrl siR + ctrl-Fc, n = 455 for ctrl siR + efnA5-Fc, n = 481 for *Ncam1* siR + ctrl-Fc, n = 495 for *Ncam1* siR + efnA5-Fc, N = 4 biological replicates). **c-f** Native ChIP revealed decreased enrichment of DNMT1 in the *Ncam1* promoter region close to putative *Snhg15-binding* sites. **c** Genomic map depicting the promoter region of the murine *Ncam1* gene. Regions targeted by the primer pairs *P1*, *P2* and *P3* are shown in turquoise, the promoter in dark blue, candidate *cis*-regulatory elements in red, CpG site with a significantly reduced methylation level in black, and putative *Snhg15*-binding sites in pink. **d-f** ChIP-qPCR analysis using anti-DNMT1 and anti-H3K27me3 antibodies normalized against the input material and IgG (N = 4 biological replicates). Significances were determined with one-way ANOVA (b) and two-tailed Student's *t*-test (d-f). Significance levels: *p* value < 0.05 *; *p* value < 0.01 **; *p* value < 0.001 ***. Scale bar: 100 μm. ctrl: control. efnA5: ephrinA5. siR: siRNA

Yildiz *et al. Epigenetics & Chromatin*   (2023) 16:42

Page 11 of 19

changes in DNMT1 enrichment were detected for a locus next to the candidate cis-regulatory element (upstream of its promoter) and in proximity to a putative *Snhg15*-binding site after ephrinA5-Fc stimulation (Additional file 1: Figure S6). In line with this, no methylation changes at CpG sites were observed for *Adamts14* (Additional file 4: Table S3). These data point to a DNA methylation-independent upregulation of *Adamts14* after ephrinA5-Fc stimulation. Neither for *Ncam1* nor for *Adamts14* locus did we observe any changes in H3K27me3 distribution in proximity of the transcriptional start site (Fig. 3d-f; Additional file 1: Figure S6b and c). Positive controls for DNMT1 and H3K27me3 are shown in Additional file 1: Figure S5e.

In sum, the *Ncam1* promoter region potentially serves as a specific target for *Snhg15*-mediated recruitment of DNMT1 and DNMT1-dependent DNA methylation, which is diminished upon ephrinA5-Fc stimulation. These results are in line with the ephrinA5-Fc triggered increased expression and reduced methylation levels of *Ncam1*.

In silico modeling points to an *Snhg15* triple helix interaction at the *Ncam1* promoter

After having shown that *Snhg15* binds DNMT1, and DNMT1 associates with the *Ncam1* promoter, with a reduction of both interactions after ephrinA5-Fc treatment, we next aimed to assess whether *Snhg15* forms a sequence-specific triple helix with the *Ncam1* locus. To this end, we performed in silico modeling in atomistic detail using molecular dynamics simulations on the sequences of *Snhg15* DBD and the previously predicted *Snhg15*-binding sites at the *Ncam1* promoter sequence (Additional file 3: Table S2). In addition, the predicted triple helix formed by *Snhg15* binding was modeled for the *Adamts14* promoter sequence. In contrast to *Ncam1*, the *Adamts14* locus did not show altered methylation levels and DNMT1 association in the promoter region (Additional file 4: Table S3).

The sequences chosen for atomistic modeling were based on predicted triple helices for *Ncam1* and *Adamts14* [34, 45] (Additional file 3: Table S2). Specifically, we have two slightly different sequences for *Adamts14* (*Adamts14*-1 and *Adamts14*-2, hereafter, see Methods for details) and for *Ncam1* (*Ncam1* and *Ncam1*-ext, hereafter, see Methods for details). All of the modeled systems are parallel triple helices, where the RNA strand (pyrimidine strand) is oriented in parallel with the purine DNA strand [83]. For the analysis, we focused on the converged parts of the trajectories (i.e., the last 400 ns, see Additional file 1: Figure S7).

We first evaluated the interaction energy between the RNA and the DNA as a sum of Lennard–Jones (LJ) and Coulomb (CB) energies. We observed that the RNA strand interacts more extensively with DNA when using the *Adamts14*-1 sequence compared to *Adamts14*-2 (Fig. 4b). The same is true for *Ncam1*-ext with respect to *Ncam1* (Fig. 4b).

We therefore tried to rationalize these trends by breaking down the molecular interactions between the nucleic acid strands. These can be classified in mainly three categories: stacking interactions between the stacked bases in each strand, cross-term interactions between non-adjacent bases across different strands, and hydrogen bonds between the strands. By evaluating the stacking and the cross-term energies of the four systems, we observed that these are comparable between *Adamts14*-1 and *Adamts14*-2 (Additional file 1: Figure S8), as well as between *Ncam1* and *Ncam1*-ext (Additional file 1: Figure S9). This suggests that the differences in stability between the systems are mainly due to the hydrogen bonding between the strands. We indeed found that *Adamts14*-1 and *Ncam1*-ext are both able to maintain on average around 27 hydrogen bonds between the RNA and the DNA helix (Fig. 4c), while *Adamts14*-2 and *Ncam1* showed only around 20 and 15 hydrogen bonds, respectively. From these data, we conclude that *Adamts14*-1 and *Ncam1*-ext are better models for simulating triple helix interaction dynamics compared to *Adamts14*-2 and *Ncam1*.

Given the key role played by hydrogen bond interactions, we decided to analyze the dynamics of hydrogen bond networks for the trajectories of *Adamts14*-1 and *Ncam1*-ext in more detail. Interestingly, the hydrogen bonding dynamics are markedly different between *Adamts14*-1 and *Ncam1*-ext, despite the very similar RNA–DNA interface (i.e., RNA–pyrimidine/DNA–purine pairs, pyr/d-pur, only interrupted by one C-dT mismatch and one G-dG mismatch, immediately followed by an A-dT pair). Specifically, we first evaluated the frequency of the so-called "*in-register*" hydrogen bonds, i.e., hydrogen bonds (H bonds) that are formed between adjacent RNA and DNA bases when the strands are aligned. For *Adamts14*-1, *in-register* H bonds are almost absent ± four base pair steps around the A–dT/G–dG double pair (Fig. 4d), whereas in *Ncam1*-ext, an almost intact *in-register* hydrogen bond network can be found in the 5'-direction (Fig. 4e). Next, *out-of-register* hydrogen bonding across the RNA and the DNA strands was also evaluated. Both *Adamts14*-1 and *Ncam1*-ext display similar and highly dynamic patterns of *out-of-register* hydrogen bonds. They form transiently and not simultaneously in different parts of the system, and with lower frequency with respect to the *in-register* ones (Additional file 1: Figure S10a and b).

Yildiz *et al. Epigenetics & Chromatin*   (2023) 16:42

Page 12 of 19
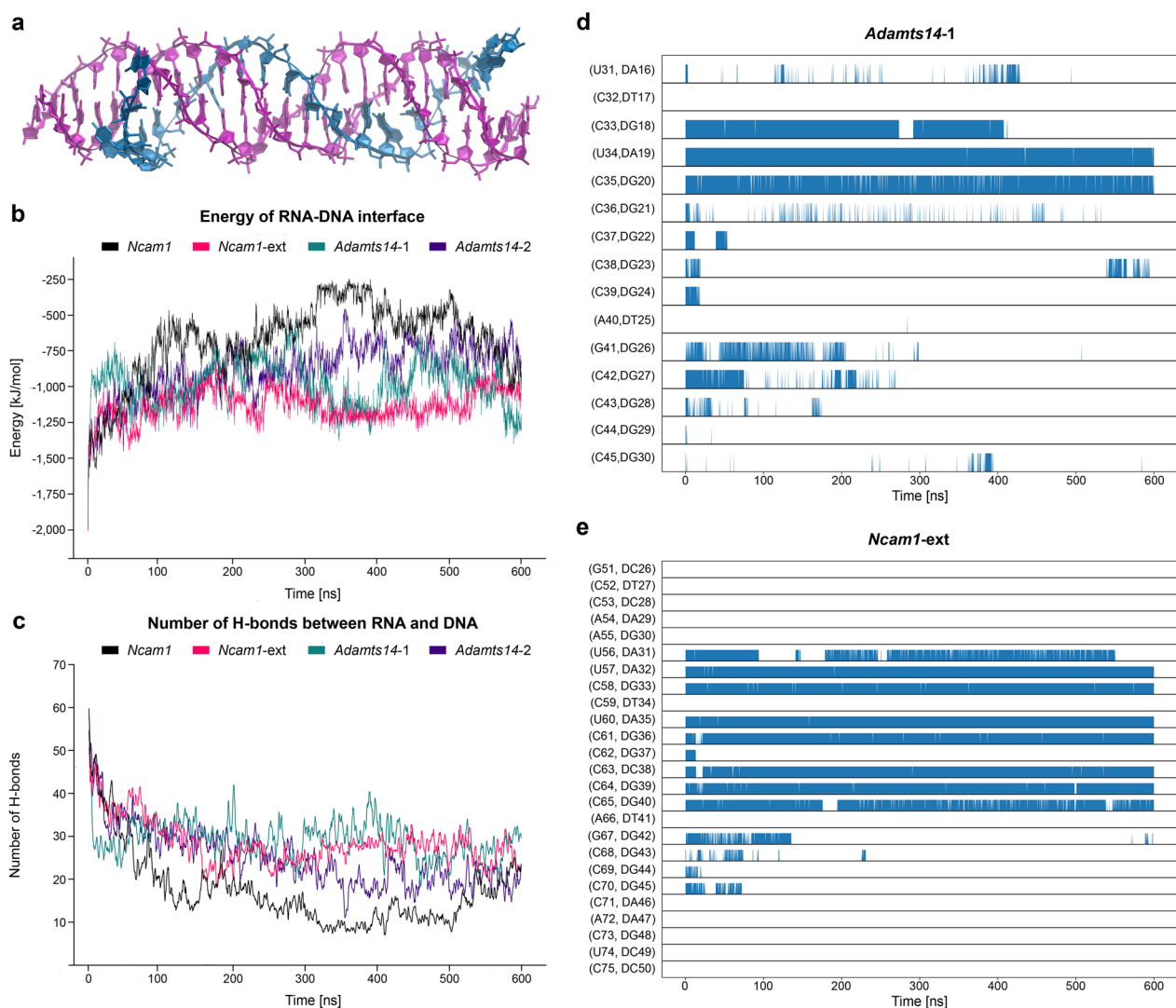
Fig. 4 In silico modeling of *Snhg15* binding to *Ncam1* and *Adamts14* promoter regions. **a** Snapshot of *Snhg15* triple helix formation with the extended *Ncam1* sequence (*Ncam1*-ext) during MD simulations. **b** Total interaction energy (LJ + CB) between DNA and RNA with phosphate and sugar backbone included as a function of time. When comparing *Ncam1* and *Ncam1*-ext, we only considered the sequence without the extension (clipped *Ncam1*-ext sequence, see Additional file 3: Table S2) to maintain comparable energies for both models. **c** Number of hydrogen bonds between RNA and DNA. Please note that the hydrogen bonds counts have been smoothed using a running average with a window size of 5, as the curves would otherwise overlap too much. Again, we only considered the sequence without the extension (clipped *Ncam1*-ext sequence) to compare *Ncam1* and *Ncam1*-ext. **d** Occurrence of *in-register* hydrogen bonded pairs between the RNA and the DNA–purine strand in *Adamts14*-1 along the simulation trajectory. Labels starting with a "D" indicate the DNA residue of the pair. **e** Occurrence of in-register hydrogen bonded pairs between the RNA and the DNA–purine strand in *Ncam1*-ext (clipped) along the simulation trajectory. Note that predicted interactions get more stable over time as indicated by less noise in the lower lanes. Labels starting with a "D" indicate the DNA residue of the pair. LJ: Lennard–Jones. CB: Coulomb

These analyses suggest that the *Ncam1* sequence has a higher probability to form a sequence-specific triple helix with *Snhg15* compared to *Adamts14*, due to its ability to establish a network of *in-register* hydrogen bonds (Fig. 4). Thus, molecular modeling supports the experimental hypothesis that *Snhg15* forms a sequence-specific triple helix with the *Ncam1* locus, enabling the recruitment of DNMT1 to this genomic site, which can be modulated by ephrinA5-Fc triggered signaling. Moreover, these findings are reflected by our molecular biology analysis which detected changes in the methylation status for *Ncam1*, but not *Adamts14* (Additional

Yildiz *et al. Epigenetics & Chromatin*   (2023) 16:42

Page 13 of 19

file 4: Table S3), and only showed DNMT1 association in the promoter region of *Ncam1*.

Discussion

We here provide evidence that ephrinA5 acts on cell motility through *Snhg15*-mediated transcriptional regulation by orchestrating DNMT1 recruitment to the *Ncam1* locus, thereby facilitating DNA methylation-dependent repression. As *Snhg15* is a cancer-related lncRNA, and CB cells serve as a model for medulloblastoma [84, 85], these findings might have impact on tumor cell biology since the Eph/ephrin system is critically involved in cancer trajectories [86].

Signals from the local microenvironment of a cell influence diverse aspects of cell intrinsic processes, key for tissue and organ development, whereas perturbations can lead to the initiation and progression of cancer [87–89]. Typically, these signals are detected by membrane receptors, such as the Eph receptor tyrosine kinases, expressed in diverse tissues including the mammalian brain, where they orchestrate neurodevelopmental processes through the regulation of critical aspects relevant for cell proliferation, differentiation, adhesion, and neuronal migration [4, 6–8, 90–92]. Furthermore, the expression of Eph receptors and ephrins as well as dysregulations in their bidirectional signaling was suggested to play a crucial role in tumor formation [93], e.g., in glioma [94] and medulloblastoma [9, 86, 95]. Thereby, ephrin-related signaling can act as both, a tumor suppressor and tumorigenic, depending on the activated downstream pathways.

The regulation of cell motility and migration is a key function of the Eph/ephrin family during organ development (e.g., the brain) as well as in cancer. Apart from an Eph/ephrin signaling-dependent modulation of actin dynamics [96], Eph receptors were shown to act on migration by mediating cell adhesion to the ECM [93, 97] through the activation of Ras homolog family member A (RhoA) via Src or the focal adhesion kinase (FAK) [98]. Here, we found an ephrinA5-dependent increase in *Ncam1* expression NCAM1 is critically implicated in establishing cell-ECM interactions and known to curtail cellular motility in health and disease [80, 81, 99].

The ephrinA5-triggered effect on CB cell motility is mediated by the EphA2 receptor. In contrast to CB cells, ephrinA5 reported increase in the motility of embryonic cortical neurons, which involves EphA4 receptor activation and signaling [6]. The same receptor was identified to mediate the repellent response which ephrinA5 triggers in migrating cortical interneurons deriving from the medial ganglionic eminence [7]. This emphasizes cell type-specific functions of ephrinA5, which could be executed by distinct receptors and downstream signaling. The relevance of the cell type- and receptor-specific functions of ephrinA5 is further underlined by other studies. While ephrinA5 enhances the migration in human hematopoietic stem and progenitor cells by binding to EphA7 [100], the same ligand negatively impacts the migration of primary hippocampal neurons in an EphA7-independent fashion [101].

Physiological effects of Eph receptor activation are further dependent on the activated downstream signaling pathways, which can be modulated by the interactions of Eph receptors with other cell surface receptors, such as the fibroblast growth factor receptor (FGFR) and chemokine receptors, as well as cell adhesion molecules such as ß-integrins [102]. This even can lead to ligand-independent receptor activation [103–105]. However, as a knockdown of EphA2 without a stimulation with ephrinA5-Fc caused no significant changes in the motility of CB cells (Additional file 1: Figure S4a and b), only the ligand-induced activation seems relevant in this context.

Due to their implication in cell motility regulation, it is not surprising that both ephrinA5 and EphA2 have been described to influence tumorigenesis and tumor progression [12, 106–108]. EphrinA5 was described to act as a tumor suppressor in glioma by negatively regulating the epidermal growth factor receptor (EGFR) [12]. In line with this, H3K27me3-mediated repression of ephrinA5 was suggested to promote tumor growth and invasion in glioblastoma multiforme (GBM) [13]. Likewise, EphA2 has been proposed as a tumor suppressor, which is upregulated at transcript and protein levels in human tissue samples and cancer cell lines [93, 109, 110]. However, EPHA2 can also act as an oncogenic protein, promoting migration, e.g., by ligand-independent activation of EPHA2 via Akt, whereas ligand-dependent activation was shown to abolish the promotion of cell motility [111], with the latter being in line with our findings.

Ephrin-triggered Eph receptor activation has been reported to converge on pathways that signal to the nucleus, such as the MAPK/ERK and PI3K-Akt/PKB pathway [102, 112]. Hence, besides remodeling focal adhesive complexes and the cytoskeleton, physiological responses (here: cell motility) could rely on induced transcriptional changes involving these pathways. Yet, so far, Eph/ephrin signaling triggered alterations in gene expression as well as the related gene regulatory mechanisms in the nucleus, are still under-investigated. Microarray-based analyses of cortical tissue from ephrinA5-deficient mice revealed essential and biologically significant transcriptional alterations [113]. Further evidence for ephrinA5-dependent modulation of gene expression was provided by Meier et al., who reported an ephrinA5-mediated suppression of the BDNF-evoked neuronal immediate early gene response [101]. Another ligand, ephrinA1, regulates hepatoma cell growth by

Yildiz *et al. Epigenetics & Chromatin* (2023) 16:42

Page 14 of 19

triggering transcriptional changes of associated genes in vitro [114]. In line with this, we identified changes in ECM- and migration-related gene expression in CB cells after 24 h of ephrinA5-Fc stimulation in a previous study [34]. Here, we report that about half of the differentially expressed genes also display changes in DNA methylation signatures, among which cell adhesion-related genes were significantly enriched. The gene coding for NCAM1, a neuronal cell adhesion molecule with key features for motility regulation in neurons as well as in cancer cells [82, 115–117], was significantly increased in expression and its promoter region showed a significant reduction in CpG methylation after ephrinA5 stimulation. Since abolishing the ephrinA5-Fc-induced increase in *Ncam1* transcript levels rescued the motility impairments, ephrinA5-triggered transcriptional changes of cell adhesion-related genes seem to be implicated mechanistically in mediating this physiological response.

In addition to its function in neurons, NCAM1 is a well-known tumor suppressor in numerous cancer types [118, 119]. *NCAM1* expression correlates positively with the survival rate in low-grade glioma patients (Additional file 1: Figure S3a). The described negative correlation of *Ncam1* expression and cell motility in the context of cancer [80–82, 99] is in line with our findings. Of note, differential promoter methylation of genes encoding for adhesion molecules, such as the epithelial cell adhesion molecule (Ep-CAM) and E-cadherin, has been frequently linked to cancer cell motility, and invasion and metastasis of cancer [120–122]. Hence, an Eph/ephrin-dependent modulation of the DNA methylome of cell adhesion-related genes, as we observed for *Ncam1*, may be a feasible mechanism of transcriptional regulation underlying reduced cellular motility in cancer cells.

LncRNAs have been implicated in the regulation of cell physiological functions, such cell proliferation, differentiation, and migration [123], in health and disease [37, 124]. LncRNAs can mediate locus-specific epigenetic remodeling by recruiting or evicting epigenetic modifiers to discrete DNA loci [40], e.g., via formation of triplex structures [46, 125, 126], and in response to environmental cues ([127, 128]). We found dysregulated expression of lncRNAs such as *Snhg15*, an important cancer-related lncRNA, in response to ephrinA5-Fc treatment. Its human orthologue *SNHG15*, which we identified to be similarly diminished in expression after ephrinA5-Fc stimulation [34], has been reported to be upregulated in multiple types of cancer. *SNHG15* participates in initiation and progression of diverse cancer types by affecting proliferation and migration [61]. The pro-oncogenic and pro-migratory function of *SNHG15* is in line with the ephrinA5-Fc-induced downregulation of *Snhg15* in CB cells, which are commonly used as a medulloblastoma cell model [34, 84], as well as the observed motility restriction. *SNHG15* has been often demonstrated to have a sponging function, binding, and disabling various miRNAs to upregulate the expression of oncogenic genes in glioma, breast cancer, and lung cancer [129–131]. Yet, RNA immunoprecipitation (RIP) assays have an *SNHG15* interaction with EZH2 to repress tumor suppressor genes via EZH2-mediated trimethylation at H3K27 in the nucleus [63]. While no such interaction between *Snhg15* and EZH2 was detected in CB cells by CLIP, which in contrast to RIP captures direct RNA–protein interactions, we found an interaction of *Snhg15* with DNMT1, a major DNA methyltransferase [132–136]. Furthermore, this interaction was reduced upon ephrinA5-Fc stimulation. DNMT1 has already been reported to interact with lncRNAs, e.g., in colon cancer, and the deregulation of DNMT1-associated lncRNAs was proposed to contribute to aberrant DNA methylation and gene expression in colon tumorigenesis [137]. Another lncRNA, *NEAT1*, interacts with DNMT1, orchestrating cytotoxic T cell infiltration in lung cancer [138]. There is increasing evidence that apart from pathophysiological conditions, DNMT–lncRNA interactions and lncRNA-mediated DNA methylation are likewise important for normal cell physiological regulation [139]. In line with this, we here provide evidence for *Snhg15*-dependent recruitment of DNMT1 to and DNA methylation of the *Ncam1* promoter region, which was abolished after ephrinA5-Fc treatment. First, we used sequence-based algorithms which consider canonical base pairing rules driving RNA–DNA triple helices [83, 140] to find potential triple helices [34]. These sequence-based methods provide hypotheses on the positions, size, and alignments of the interaction patterns that are parameters necessary to build targeted all atom models, which then provide further insights into the physics of the interaction, such as stability, dynamics, and role of individual nucleotides.

Next, atomistic models were constructed based on the predicted binding site alignments. Specifically, atomistic model not only helped in selecting the most stable triple helix among the ones predicted for both *Adamts14* and *Ncam1*, but also, their ability to establish specific interactions with *Snhg15* was evaluated. Molecular dynamic simulations suggest that while the selected triple helices for *Ncam1* and *Adamts14* display a comparable overall stability, the local interaction established at the RNA–DNA interface is significantly different. *Ncam1* indeed features several *in-register* hydrogen bonds, persistent over the entire simulations time, that maintain the sequence-specific complementary of hydrogen bond networks between the RNA–DNA triplex interfaces. This is not the case for *Adamts14* where the lack of persistent *in-register* hydrogen bonds suggests a less sequence-specific

Yildiz *et al. Epigenetics & Chromatin*   (2023) 16:42

Page 15 of 19

interaction between RNA and DNA. Such results are in line with our wet lab approaches: for the *Ncam1* but not for *Adamts14* promoter region significant change in methylation levels were detected in response to the ephrinA5-Fc treatment (Additional file 6).

There are only a few simulations of RNA/DNA interaction via triple helix formation [46, 140]. Optimizing model details and parameters for such molecular dynamics simulations, such as the protonation state and appropriate force fields, remains an active area of research [141] which is yet still hampered by the—so far—low number of physical experiments on these molecules.

The lncRNA-mediated targeting of epigenetic writers such as DNMTs or histone-modifying proteins represents an attractive mechanism for dysregulation of epigenetic signatures that occurs in cancer cells. This finding seems to be specifically relevant since the regulation of lncRNA expression is responsive to signaling from peripheral membrane receptors commonly reported in cancer, including the Eph/ephrin signaling [34]. However, how (other) distinct lncRNAs are affected in their transcription in response to, e.g., ephrin stimulation or neuronal activity, and which signaling pathways are involved, needs to be dissected in future studies.

Supplementary Information

The online version contains supplementary material available at https://doi.org/10.1186/s13072-023-00516-4.

Additional file 1: Figure S1. Western blots confirming the specificity of antibodies against DNMT1 and EZH2. (a) Immunoprecipitations from N2a whole cell lysate with normal rabbit IgG (#12–370, Merck) and rabbit anti-DNMT1 (#70–201, BioAcademia) antibodies. Detection was performed with the mouse anti-DNMT1 antibody (1:250, # ab13537, abcam). (b) The EZH2 antibody (1:1000, #5246, Cell Signaling Technology) was used for detection on whole cell lysate from the murine medial ganglionic eminence (MGE). Protein sizes are indicated in kDa, identified through SERVA Protein standard III. **Figure S2.** CLIP revealed no interaction of Snhg15 and EZH2 in CB cells. RNA recovery for IgG and anti-EZH2 antibody CLIP samples in CB cells (N = 5 biological replicates). For all investigated amplicons, the recovery for EZH2 could not be statistically differentiated from the IgG-based pulldown. Whiskers of the box plots extend 1.5 times the interquartile range from the 25th and 75th percentiles (Tukey style) while outliers are represented by hollow dots. Significances were determined with two-tailed Student's t-test. ctrl-Fc: control-Fc, efnA5-Fc: ephrinA5-Fc, CB: cerebellar granule, CLIP: UV cross-linking and immunoprecipitation. **Figure S3.** Expression of *NCAM1*/*Ncam1* is implicated in low-grade glioma as well as the migration of CB cells, where it can be downregulated via RNA silencing. (a) High expression levels of *NCAM1* are associated with increased patient survival in low-grade glioma. Survival analysis is based on clinical data and gene expression counts from tumor samples of lower grade glioma patients downloaded from BioPortal (http://www.cbioportal.org/study/clinicalData?id=lgg_tcga) and The Cancer Genome Atlas (TCGA), respectively. (b) Knockdown efficiency of the applied *Ncam1* siRNA (N = 3 biological replicates). (c) Quantitative analysis of migration distance of CB cells (n = 557 for ctrl siR + ctrl-Fc, n = 455 for ctrl siR + efnA5-Fc, n = 481 for Ncam1 siR + ctrl-Fc, n = 495 for Ncam1 siR + efnA5-Fc, N = 4 biological replicates). Significances were determined with log-rank (a), Wilcoxon–Mann–Whitney test (b) and one-way ANOVA (c). Significance levels: *p* value < 0.05 *; *p* value < 0.01 **; *p* value < 0.001 ***. ctrl: control. efnA5:

ephrinA5. LGG: low-grade glioma. siR: siRNA. **Figure S4.** Migratory analysis of CB cells upon stimulation with ephrinA5-Fc and downregulation of *EphA2*. The motility of CB cells was reduced upon stimulation with ephrinA5-Fc. (a) Temporal color-coded migratory distance over 20 h of imaging. The starting point of migration for each cell is shown in dark blue and the end point in white. (b) Quantitative analysis of average migratory speed (n = 268 for ctrl siR + ctrl-Fc, n = 244 for ctrl siR + efnA5-Fc, n = 273 for *EphA2* siR + ctrl-Fc, n = 238 for *EphA2* siR + efnA5-Fc, N = 3 biological replicates). (c) Knockdown efficiency of the applied *EphA2*-siRNA (N = 3 biological replicates). Significances were determined with one-way ANOVA (b) and Wilcoxon-Mann–Whitney test (c). Significance levels: *p* value < 0.05 *; *p* value < 0.01 **; *p* value < 0.001 ***. Scale bar: 100 μm. ctrl: control. efnA5: ephrinA5. siR: siRNA. **Figure S5.** The murine *Ncam1* locus shows bivalent regulation in primary cerebellar tissue and CB cells. (a) The peaks depict publicly available ChIP-seq data for H3K27me3 and H3K4me3 in the murine *Ncam1* locus in cerebellar tissue from various developmental stages. The corresponding GEO accession numbers for the datasets from top to bottom are as follows: GSM1000143, GSE29184, GSM1000090, GSM769027. Genomic regions targeted by the primers are shown in turquoise. The promoter is shown in dark blue, candidate cis-regulatory elements in red, CpG islands in green, and putative *Snhg15*-binding sites in pink. (b-d) Native ChIP using anti-DNMT1 and anti-H3K27me3 with qPCR analysis targeting the *Ncam1* promoter region normalized against the input material and IgG (N = 4 biological replicates). Stimulation of CB cells with ephrinA5-Fc does not alter the DNMT1 or H3K4me3 enrichment within the *Ncam1* locus (b-d). (e) Native ChIP using anti-DNMT1, anti-H3K27me3 and anti-H3K4me3 with qPCR analysis targeting the muscle differentiation gene *MyoD* normalized against the input material and IgG (N = 4 biological replicates). The *MyoD* locus is enriched with DNMT1 and the repressive histone mark H3K27me3 but lacks the permissive histone mark H3K4me3 in CB cells. The results were tested for statistical significance with a two-tailed Student's t-test (b-e). CB: cerebellar granule. ctrl: control. E14.5: embryonic day 14.5. efnA5: ephrinA5. P0: post-natal day 0. W8: post-natal week 8. **Figure S6.** Native ChIP reveals no changes in DNMT1 association and histone methylation signatures within the proximity of a *cis*-regulatory element of *Adamts14* and the putative *Snhg15*-binding sites. (a) Genomic regions targeted by the primers are shown in turquoise. The promoter is shown in dark blue, candidate cis-regulatory elements in red, and putative *Snhg15*-binding sites in pink. (b-c) ChIP-qPCR analysis with anti-DNMT1 and anti-H3K27me3 antibodies for the promoter region of *Adamts14* normalized against the input material and IgG (N = 3 biological replicates for *P1* (b), N = 4 biological replicates for *P2* (c)). Significances were determined with two-tailed Student's t-test. Significance levels: *p* value < 0.05 *; *p* value < 0.01 **; *p* value < 0.001 ***. ctrl: control. efnA5: ephrinA5. **Figure S7.** Root mean square deviation (RMSD) plot for *Ncam1*, *Ncam1*-ext, *Adamts14*-1 and *Adamts14*-2 taken over the entire trajectory of 600 ns for (a) the RNA strand of the triple helix and (b) the DNA double helix. **Figure S8.** Comparison of energy contributions between the two *Adamts14* models (*Adamts14*-1 and *Adamts14*-2). The hydrogen bond energies between individual residues at the same base pair level (i) were calculated by taking the sum of Lennard–Jones (LJ) and Coulomb (CB) short-range interaction energies. The cross-energies were calculated for a base pair level (i) by considering the sum of LJ and CB short-range interaction energies of (i)th residue in chain B with (i + 1) th and (i-1)th residue in chain A and C. The stacking energies were calculated for a base pair step level by considering the sum of LJ and CB short-range interaction energies of (i)th and (i + 1)th residues in chain A, B, and C. The total plot shows the sum of the contribution of individual energies at the (i)th base pair level. In all calculations, the energy contributions involving terminal residues were not included to avoid discrepancy in the number of terms that contribute. **Figure S9.** Comparison of energy contributions between the two *Ncam1* models (*Ncam1* and *Ncam1*-ext). The hydrogen bond energies between individual residues at the same base pair level (i) were calculated by taking the sum of Lennard–Jones (LJ) and Coulomb (CB) short-range

Yildiz *et al. Epigenetics & Chromatin* (2023) 16:42

Page 16 of 19

interaction energies. The cross-energies were calculated for a base pair level (i) by considering the sum of LJ and CB short-range interaction energies of (i)th residue in chain B with (i + 1)th and (i-1)th residue in chain A and C. The stacking energies were calculated for a base pair step level by considering the sum of LJ and CB short-range interaction energies of the (i)th and (i + 1)th residue in chain A, B, and C. The total plot shows the sum of the contribution of individual energies at the (i)th base pair level. In all calculations the energy contributions involving terminal residues were not included to avoid discrepancy in the number of terms that contribute. **Figure S10.** Display of all hydrogen bonded interactions of the RNA that occur with frequency > 1% in the (a) *Adamts14*-1 and (b) *Ncam1*-ext simulation. For clarity the purine DNA strand was drawn above, and the pyrimidine DNA strand below the RNA. H bonds between the two DNA strands as well as within individual strands are omitted to focus on the H bond patterns of the RNA strand. Occurrence is in "H bond units", i.e., an occurrence of > 100% indicates that on average there exists more than one H bond between the respective residues.

Additional file 2: Table S1. Sequences of applied primer pairs in (RT-)qPCR experiments.

Additional file 3: Table S2. Detailed sequences of the simulated systems (*Adamts14*-1, *Adamts14*-2, *Ncam1*, *Ncam1*-ext). Pairing between DNA sequences (black) and RNA sequences (red) is predicted to form triple helixes for two binding sites in the *Adamts14* promoter and one binding site at the *Ncam1* promoter. 5′ and 3′ indicates the orientation of the DNA and RNA strands. "|" indicates base pairing following triple helix canonical code, while "*" indicates positions with a mismatch.

Additional file 4: Table S3. Differentially methylated sites in CB cells treated with ephrinA5-Fc. Table lists all probes/sites (DMSs) with an adjusted p value ≤ 0.05 (adj. pval). Output of the function minfi::dmpFinder() for identified differentially methylated sites in CB cells treated with ephrinA5-Fc. The minfi::dmpFinder() function models the methylation ß-value of the respective CpG for each phenotype (i.e., "efnA5" or "control") with linear regression model and then determines whether the two regression models differ significantly from each other by use of an F-test. The table shows the parameters of the fitted regression models and the results of the F-test for all probes/sites (DMSs) with an adjusted p value ≤ 0.05 (adj. pval).

Additional file 5: Table S4. Table depicts all 19 protein-coding genes upregulated after 24 h ephrinA5-Fc treatment and with putative triplex target DNA sites (TTS) for *Snhg15* (RNA-seq; Pensold et al. 2021).

Additional file 6. Additional methods.

Author contributions

CBY performed experiments and data analysis, figure illustration, assisted in writing the manuscript; TK atomistic modeling, data analysis; JG bioinformatic analysis; JK performed experiments and data analysis; AR performed experiments; PW performed experiments; FK data analysis; TM data analysis; MJ statistical analysis, figure illustration; DP method development, performed experiments; OZ atomistic modeling, data discussion; GR atomistic modeling, data discussion; IC assistance in computational analysis, data discussion; GZB conceptual design, wrote the manuscript, data discussion.

Availability of data and materials

The dataset(s) supporting the conclusions of this article are included as additional files and the Illumina Mouse Methylation BeadChIP data is available in the GEO-NCBI repository, with the GEO number GSE229001; https://www.ncbi.nlm.nih.gov/geo/query/acc.cgi?acc=GSE229001.

Declarations

Ethics approval and consent to participate
Not applicable.

Consent for publication
Not applicable.

Competing interests
Not applicable.

Author details
[1]Institute of Zoology (Biology 2), Division of Neuroepigenetics, RWTH Aachen University, Worringerweg 3, 52074 Aachen, Germany. [2]Research Training Group 2416 Multi Senses – Multi Scales, RWTH Aachen University, 52074 Aachen, Germany. [3]Jülich Supercomputing Centre, Forschungszentrum Jülich GmbH, 52425 Jülich, Germany. [4]Institute for Computational Genomics, RWTH Aachen University, Medical Faculty, 52074 Aachen, Germany. [5]Department of Neurosciences and Rehabilitation, Section of Medical Biochemistry, Molecular Biology and Genetics, University of Ferrara, Ferrara, Italy. [6]Institute for Human Genetics and Genomic Medicine, Medical Faculty, RWTH Aachen University, 52074 Aachen, Germany. [7]Department of Neurology, University Hospital Aachen, RWTH Aachen University, Aachen, Germany. [8]Institute of Neuroscience and Medicine (INM-9)/Institute of Advanced Simulations (IAS-5), Forschungszentrum Jülich GmbH, 52425 Jülich, Germany.

References

1. Spill F, Reynolds DS, Kamm RD, Zaman MH. Impact of the physical microenvironment on tumor progression and metastasis. Curr Opin Biotechnol. 2016;40:41–8.
2. Eisenberg L, Eisenberg-Bord M, Eisenberg-Lerner A, Sagi-Eisenberg R. Metabolic alterations in the tumor microenvironment and their role in oncogenesis. Cancer Lett. 2020;484:65–71.
3. Manzo G. Similarities between embryo development and cancer process suggest new strategies for research and therapy of tumors: a new point of view. Front Cell Develop Biol. 2019;7:20.
4. Gerstmann K, Pensold D, Symmank J, Khundadze M, Hübner CA, Bolz J, Zimmer G. Thalamic afferents influence cortical progenitors via ephrin A5-EphA4 interactions. Development. 2015;142(1):140–50.
5. Steinecke A, Gampe C, Zimmer G, Rudolph J, Bolz J. EphA/ephrin A reverse signaling promotes the migration of cortical interneurons from the medial ganglionic eminence. Development. 2014;141(2):460–71.
6. Zimmer G, Kästner B, Weth F, Bolz J. Multiple effects of ephrin-A5 on cortical neurons are mediated by SRC family kinases. J Neurosci. 2007;27(21):5643–53.
7. Zimmer G, Garcez P, Rudolph J, Niehage R, Weth F, Lent R, Bolz J. Ephrin-A5 acts as a repulsive cue for migrating cortical interneurons. Eur J Neurosci. 2008;28(1):62–73.
8. Zimmer G, Rudolph J, Landmann J, Gerstmann K, Steinecke A, Gampe C, Bolz J. Bidirectional ephrinB3/EphA4 signaling mediates the segregation of medial ganglionic eminence-and preoptic area-derived interneurons in the deep and superficial migratory stream. J Neurosci. 2011;31(50):18364–80.
9. Sikkema AH, Den Dunnen WF, Hulleman E, Van Vuurden DG, Garcia-Manero G, Yang H, et al. EphB2 activity plays a pivotal role in

Yildiz *et al. Epigenetics & Chromatin*   (2023) 16:42

Page 17 of 19

pediatric medulloblastoma cell adhesion and invasion. Neuro Oncol. 2012;14(9):1125–35.

10. Surawska H, Ma PC, Salgia R. The role of ephrins and Eph receptors in cancer. Cytokine Growth Factor Rev. 2004;15(6):419–33.

11. Uddin MS, Al Mamun A, Alghamdi BS, Tewari D, Jeandet P, Sarwar MS, Ashraf GM, editors. Epigenetics of Glioblastoma Multiforme: From Molecular Mechanisms to Therapeutic Approaches; 2020: Elsevier.

12. Li J-J, Liu D-P, Liu G, Xie D. EphrinA5 acts as a tumor suppressor in glioma by negative regulation of epidermal growth factor receptor. Oncogene. 2009;28(15):1759–68.

13. Ricci B, Millner TO, Pomella N, Zhang X, Guglielmi L, Badodi S, et al. Polycomb-mediated repression of EphrinA5 promotes growth and invasion of glioblastoma. Oncogene. 2020;39(12):2523–38.

14. Hamaoka Y, Negishi M, Katoh H. EphA2 is a key effector of the MEK/ERK/RSK pathway regulating glioblastoma cell proliferation. Cell Signal. 2016;28(8):937–45.

15. Wykosky J, Debinski W. The EphA2 receptor and ephrinA1 ligand in solid tumors: function and therapeutic targeting. Mol Cancer Res. 2008;6(12):1795–806.

16. Wykosky J, Gibo DM, Stanton C, Debinski W. EphA2 as a novel molecular marker and target in glioblastoma multiforme. Mol Cancer Res. 2005;3(10):541–51.

17. Anastasiadou E, Jacob LS, Slack FJ. Non-coding RNA networks in cancer. Nat Rev Cancer. 2018;18(1):5–18.

18. Esteller M. Epigenetics in cancer. N Engl J Med. 2008;358(11):1148–59.

19. Sharma S, Kelly TK, Jones PA. Epigenetics in cancer. Carcinogenesis. 2010;31(1):27–36.

20. Phillips RE, Soshnev AA, Allis CD. Epigenomic reprogramming as a driver of malignant glioma. Cancer Cell. 2020;38(5):647–60.

21. Laurent L, Wong E, Li G, Huynh T, Tsirigos A, Ong CT, et al. Dynamic changes in the human methylome during differentiation. Genome Res. 2010;20(3):320–31.

22. Liu XS, Wu H, Ji X, Stelzer Y, Wu X, Czauderna S, et al. Editing DNA methylation in the mammalian genome. Cell. 2016;167(1):233–47.

23. Stepper P, Kungulovski G, Jurkowska RZ, Chandra T, Krueger F, Reinhardt R, et al. Efficient targeted DNA methylation with chimeric dCas9–Dnmt3a–Dnmt3L methyltransferase. Nucleic Acids Res. 2017;45(4):1703–13.

24. Al-Kharashi LA, Al-Mohanna FH, Tulbah A, Aboussekhra A. The DNA methyl-transferase protein DNMT1 enhances tumor-promoting properties of breast stromal fibroblasts. Oncotarget. 2018;9(2):2329.

25. Gusyatiner O, Hegi ME, editors. Glioma epigenetics: from subclassification to novel treatment options; 2018: Elsevier.

26. Fuks F, Burgers WA, Brehm A, Hughes-Davies L, Kouzarides T. DNA methyltransferase Dnmt1 associates with histone deacetylase activity. Nat Genet. 2000;24(1):88–91.

27. Symmank J, Bayer C, Reichard J, Pensold D, Zimmer-Bensch G. Neuronal Lhx1 expression is regulated by DNMT1-dependent modulation of histone marks. Epigenetics. 2020;15(11):1259–74.

28. Guo JU, Ma DK, Mo H, Ball MP, Jang M-H, Bonaguidi MA, et al. Neuronal activity modifies the DNA methylation landscape in the adult brain. Nat Neurosci. 2011;14(10):1345–51.

29. Guo H, Zhu P, Yan L, Li R, Hu B, Lian Y, et al. The DNA methylation landscape of human early embryos. Nature. 2014;511(7511):606–10.

30. Skvortsova K, Stirzaker C, Taberlay P. The DNA methylation landscape in cancer. Essays Biochem. 2019;63(6):797–811.

31. Yildiz CB, Zimmer-Bensch G. Role of DNMTs in the Brain. DNA Methyl-transferases-Role and Function: Springer; 2022. p. 363–94.

32. Hua C-D, Bian E-B, Chen E-F, Yang Z-H, Tang F, Wang H-L, Zhao B. Repression of Dok7 expression mediated by DNMT1 promotes glioma cells proliferation. Biomed Pharmacother. 2018;106:678–85.

33. Sun J, Tian X, Zhang J, Huang Y, Lin X, Chen L, Zhang S. Regulation of human glioma cell apoptosis and invasion by miR-152-3p through targeting DNMT1 and regulating NF2. J Exp Clin Cancer Res. 2017;36(1):1–13.

34. Pensold D, Gehrmann J, Pitschelatow G, Walberg A, Braunsteffer K, Reichard J, et al. The Expression of the Cancer-Associated lncRNA Snhg15 Is Modulated by EphrinA5-Induced Signaling. Int J Mol Sci. 2021;22(3):1332.

35. Laneve P, Rea J, Caffarelli E. Long noncoding RNAs: emerging players in medulloblastoma. Front Pediatr. 2019;7:67.

36. Stackhouse CT, Gillespie GY, Willey CD. Exploring the roles of lncRNAs in GBM pathophysiology and their therapeutic potential. Cells. 2020;9(11):2369.

37. Jiang M-C, Ni J-J, Cui W-Y, Wang B-Y, Zhuo W. Emerging roles of lncRNA in cancer and therapeutic opportunities. Am J Cancer Res. 2019;9(7):1354.

38. Ghafouri-Fard S, Esmaeili M, Taheri M. H19 lncRNA: roles in tumorigenesis. Biomed Pharmacother. 2020;123:109774.

39. Yadav B, Pal S, Rubstov Y, Goel A, Garg M, Pavlyukov M, Pandey AK. LncRNAs associated with glioblastoma: from transcriptional noise to novel regulators with a promising role in therapeutics. Molecular Therapy-Nucleic Acids. 2021;24:728–42.

40. Zimmer-Bensch G. Emerging roles of long non-coding RNAs as drivers of brain evolution. Cells. 2019;8(11):1399.

41. Marchese FP, Raimondi I, Huarte M. The multidimensional mechanisms of long noncoding RNA function. Genome Biol. 2017;18:1–13.

42. Cabianca DS, Casa V, Bodega B, Xynos A, Ginelli E, Tanaka Y, Gabellini D. A long ncRNA links copy number variation to a polycomb/trithorax epigenetic switch in FSHD muscular dystrophy. Cell. 2012;149(4):819–31.

43. Rinn JL, Kertesz M, Wang JK, Squazzo SL, Xu X, Brugmann SA, et al. Functional demarcation of active and silent chromatin domains in human HOX loci by noncoding RNAs. Cell. 2007;129(7):1311–23.

44. Kalwa M, Hänzelmann S, Otto S, Kuo C-C, Franzen J, Joussen S, et al. The lncRNA HOTAIR impacts on mesenchymal stem cells via triple helix formation. Nucleic Acids Res. 2016;44(22):10631–43.

45. Kuo C-C, Hänzelmann S, Sentürk Cetin N, Frank S, Zajzon B, Derks J-P, et al. Detection of RNA–DNA binding sites in long noncoding RNAs. Nucleic Acids Res. 2019;47(6):e32.

46. Leisegang MS, Bains JK, Seredinski S, Oo JA, Krause NM, Kuo C-C, et al. HIF1α-AS1 is a DNA: DNA: RNA triplex-forming lncRNA interacting with the HUSH complex. Nat Commun. 2022;13(1):6563.

47. Sentürk Cetin N, Kuo C-C, Ribarska T, Li R, Costa IG, Grummt I. Isolation and genome-wide characterization of cellular DNA: RNA triplex structures. Nucleic Acids Res. 2019;47(5):2306–21.

48. Fossale E, Wolf P, Espinola JA, Lubicz-Nawrocka T, Teed AM, Gao H, et al. Membrane trafficking and mitochondrial abnormalities precede subunit c deposition in a cerebellar cell model of juvenile neuronal ceroid lipofuscinosis. BMC Neurosci. 2004;5(1):1–13.

49. Sharma P, Lam VK, Raub CB, Chung BM. Tracking Single Cells Motility on Different Substrates. Methods Protocols. 2020;3(3):56.

50. Livak KJ, Schmittgen TD. Analysis of relative gene expression data using real-time quantitative PCR and the 2− ΔΔCT method. Methods. 2001;25(4):402–8.

51. Lee FCY, Ule J. Advances in CLIP Technologies for Studies of Protein-RNA Interactions. Mol Cell. 2018;69(3):354–69. https://doi.org/10.1016/j.molcel.2018.01.005.

52. Xu Z, Niu L, Li L, Taylor JA. ENmix: a novel background correction method for Illumina HumanMethylation450 BeadChip. Nucleic Acids Res. 2016;44(3):e20. https://doi.org/10.1093/nar/gkv907.

53. Leek JT. Surrogate variable analysis. Washington: University of Washington; 2007.

54. Aryee MJ, Jaffe AE, Corrada-Bravo H, Ladd-Acosta C, Feinberg AP, Hansen KD, Irizarry RA. Minfi: a flexible and comprehensive Bioconductor package for the analysis of Infinium DNA methylation microarrays. Bioinformatics. 2014;30(10):1363–9.

55. Ivani I, Dans PD, Noy A, Pérez A, Faustino I, Hospital A, et al. Parmbsc1: a refined force field for DNA simulations. Nat Methods. 2016;13(1):55–8.

56. Piana S, Donchev AG, Robustelli P, Shaw DE. Water dispersion interactions strongly influence simulated structural properties of disordered protein states. J Phys Chem B. 2015;119(16):5113–23.

57. Joung IS, Cheatham TE III. Determination of alkali and halide monovalent ion parameters for use in explicitly solvated biomolecular simulations. J Phys Chem B. 2008;112(30):9020–41.

58. Abraham MJ, Murtola T, Schulz R, Páll S, Smith JC, Hess B, Lindahl E. GROMACS: High performance molecular simulations through multi-level parallelism from laptops to supercomputers. SoftwareX. 2015;1:19–25.

59. Parrinello M, Rahman A. Polymorphic transitions in single crystals: A new molecular dynamics method. J Appl Phys. 1981;52(12):7182–90.

Yildiz *et al. Epigenetics & Chromatin*   (2023) 16:42

Page 18 of 19

60. Hess B. P-LINCS: A parallel linear constraint solver for molecular simulation. J Chem Theory Comput. 2008;4(1):116–22.

61. Tong J, Ma X, Yu H, Yang J. SNHG15: a promising cancer-related long noncoding RNA. Cancer Manag Res. 2019;11:5961.

62. Wu D-M, Wang S, Wen X, Han X-R, Wang Y-J, Shen M, et al. LncRNA SNHG15 acts as a ceRNA to regulate YAP1-Hippo signaling pathway by sponging miR-200a-3p in papillary thyroid carcinoma. Cell Death Dis. 2018;9(10):947.

63. Ma Z, Huang H, Wang J, Zhou Y, Pu F, Zhao Q, et al. Long non-coding RNA SNHG15 inhibits P15 and KLF2 expression to promote pancreatic cancer proliferation through EZH2-mediated H3K27me3. Oncotarget. 2017;8(48):84153.

64. Chalei V, Sansom SN, Kong L, Lee S, Montiel JF, Vance KW, Ponting CP. The long non-coding RNA Dali is an epigenetic regulator of neural differentiation. Elife. 2014;3:e04530.

65. Guil S, Soler M, Portela A, Carrère J, Fonalleras E, Gómez A, et al. Intronic RNAs mediate EZH2 regulation of epigenetic targets. Nat Struct Mol Biol. 2012;19(7):664–70.

66. Wang L, Zhao Y, Bao X, Zhu X, Kwok YK, Sun K, et al. LncRNA Dum interacts with Dnmts to regulate Dppa2 expression during myogenic differentiation and muscle regeneration. Cell Res. 2015;25(3):335–50.

67. Cao R, Wang H, He J, Erdjument-Bromage H, Tempst P, Zhang Y. Role of hPHF1 in H3K27 methylation and Hox gene silencing. Mol Cell Biol. 2008;28(5):1862–72. https://doi.org/10.1128/mcb.01589-07.

68. Kuzmichev A, Nishioka K, Erdjument-Bromage H, Tempst P, Reinberg D. Histone methyltransferase activity associated with a human multiprotein complex containing the Enhancer of Zeste protein. Genes Dev. 2002;16(22):2893–905. https://doi.org/10.1101/gad.1035902.

69. Margueron R, Reinberg D. The Polycomb complex PRC2 and its mark in life. Nature. 2011;469(7330):343–9.

70. Zemach A, McDaniel IE, Silva P, Zilberman D. Genome-wide evolutionary analysis of eukaryotic DNA methylation. Science. 2010;328(5980):916–9.

71. Chen Y, Hou S, Jiang R, Sun J, Cheng C, Qian Z. EZH2 is a potential prognostic predictor of glioma. J Cell Mol Med. 2021;25(2):925–36.

72. Hervouet E, Vallette F, Cartron P. Impact of the DNA methyltransferases expression on the methylation status of apoptosis-associated genes in glioblastoma multiforme. Cell Death Dis. 2010;1(1):e8.

73. Miele E, Valente S, Alfano V, Silvano M, Mellini P, Borovika D, et al. The histone methyltransferase EZH2 as a druggable target in SHH medulloblastoma cancer stem cells. Oncotarget. 2017;8(40):68557.

74. Pócza T, Krenács T, Turányi E, Csáthy J, Jakab Z, Hauser P. High expression of DNA methyltransferases in primary human medulloblastoma. 2016.

75. Rajendran G, Shanmuganandam K, Bendre A, Mujumdar D, Goel A, Shiras A. Epigenetic regulation of DNA methyltransferases: DNMT1 and DNMT3B in gliomas. J Neurooncol. 2011;104(2):483–94.

76. Stazi G, Taglieri L, Nicolai A, Romanelli A, Fioravanti R, Morrone S, et al. Dissecting the role of novel EZH2 inhibitors in primary glioblastoma cell cultures: effects on proliferation, epithelial-mesenchymal transition, migration, and on the pro-inflammatory phenotype. Clin Epigenetics. 2019;11(1):1–17.

77. Zhang H, Zhu D, Zhang Z, Kaluz S, Yu B, Devi NS, et al. EZH2 targeting reduces medulloblastoma growth through epigenetic reactivation of the BAI1/p53 tumor suppressor pathway. Oncogene. 2020;39(5):1041–8.

78. Li E, Bestor TH, Jaenisch R. Targeted mutation of the DNA methyltransferase gene results in embryonic lethality. Cell. 1992;69(6):915–26.

79. Jones PA. Functions of DNA methylation: islands, start sites, gene bodies and beyond. Nat Rev Genet. 2012;13(7):484–92.

80. Prag S, Lepekhin EA, Kolkova K, Hartmann-Petersen R, Kawa A, Walmod PS, et al. NCAM regulates cell motility. J Cell Sci. 2002;115(2):283–92.

81. Edvardsen K, Pedersen PH, Bjerkvig R, Hermann GG, Zeuthen J, Laerum OD, et al. Transfection of glioma cells with the neural-cell adhesion molecule NCAM: effect on glioma-cell invasion and growth in vivo. Int J Cancer. 1994;58(1):116–22.

82. Guan G, Niu X, Qiao X, Wang X, Liu J, Zhong M. Upregulation of neural cell adhesion molecule 1 (NCAM1) by hsa-miR-141-3p suppresses ameloblastoma cell migration. Med Sci Monit. 2020;26:e923491–501.

83. Buske FA, Mattick JS, Bailey TL. Potential in vivo roles of nucleic acid triple-helices. RNA Biol. 2011;8(3):427–39. https://doi.org/10.4161/rna.8.3.14999.

84. Behesti H, Marino S. Cerebellar granule cells: insights into proliferation, differentiation, and role in medulloblastoma pathogenesis. Int J Biochem Cell Biol. 2009;41(3):435–45.

85. Gilbertson RJ, Ellison DW. The origins of medulloblastoma subtypes. Annu Rev Pathol Mech Dis. 2008;3:341–65.

86. Anderton M, van der Meulen E, Blumenthal MJ, Schäfer G. The Role of the Eph Receptor Family in Tumorigenesis. Cancers. 2021;13(2):206. https://doi.org/10.3390/cancers13020206.

87. Casal JJ. Environmental cues affecting development. Curr Opin Plant Biol. 2002;5(1):37–42.

88. Herceg Z, Vaissière T. Epigenetic mechanisms and cancer: an interface between the environment and the genome. Epigenetics. 2011;6(7):804–19.

89. Parsa N. Environmental factors inducing human cancers. Iran J Public Health. 2012;41(11):1.

90. Rudolph J, Zimmer G, Steinecke A, Barchmann S, Bolz J. Ephrins guide migrating cortical interneurons in the basal telencephalon. Cell Adh Migr. 2010;4(3):400–8.

91. Rudolph J, Gerstmann K, Zimmer G, Steinecke A, Döding A, Bolz J. A dual role of EphB1/ephrin-B3 reverse signaling on migrating striatal and cortical neurons originating in the preoptic area: should I stay or go away? Front Cell Neurosci. 2014;8:185.

92. Gerstmann K, Zimmer G. The role of the Eph/ephrin family during cortical development and cerebral malformations. Med Res Arch. 2018;6(3):78.

93. Pasquale EB. Eph receptors and ephrins in cancer: bidirectional signalling and beyond. Nat Rev Cancer. 2010;10(3):165–80.

94. Ferluga S, Debinski W. Ephs and Ephrins in malignant gliomas. Growth Factors. 2014;32(6):190–201.

95. Bhatia S, Hirsch K, Baig NA, Rodriguez O, Timofeeva O, Kavanagh K, et al. Effects of altered ephrin-A5 and EphA4/EphA7 expression on tumor growth in a medulloblastoma mouse model. J Hematol Oncol. 2015;8(1):1–8.

96. Kindberg AA, Srivastava V, Muncie JM, Weaver VM, Gartner ZJ, Bush JO. EPH/EPHRIN regulates cellular organization by actomyosin contractility effects on cell contacts. J Cell Biol. 2021;220(6). https://doi.org/10.1083/jcb.202005216.

97. Nakada M, Niska JA, Tran NL, McDonough WS, Berens ME. EphB2/R-Ras signaling regulates glioma cell adhesion, growth, and invasion. Am J Pathol. 2005;167(2):565–76.

98. Wang J, Zheng X, Peng Q, Zhang X, Qin Z. Eph receptors: the bridge linking host and virus. Cell Mol Life Sci. 2020;77(12):2355–65.

99. Blaheta RA, Hundemer M, Mayer G, Vogel JU, Kornhuber B, Cinatl J, et al. Expression level of neural cell adhesion molecule (NCAM) inversely correlates with the ability of neuroblastoma cells to adhere to endothelium in vitro. Cell Commun Adhes. 2002;9(3):131–47. https://doi.org/10.1080/15419060214520.

100. Nguyen TM, Arthur A, Zannettino AC, Gronthos S. EphA5 and EphA7 forward signaling enhances human hematopoietic stem and progenitor cell maintenance, migration, and adhesion via Rac1 activation. Exp Hematol. 2017;48:72–8.

101. Meier C, Anastasiadou S, Knöll B. Ephrin-A5 suppresses neurotrophin evoked neuronal motility, ERK activation and gene expression. PLoS ONE. 2011;6(10):e26089.

102. Arvanitis D, Davy A. Eph/ephrin signaling: networks. Genes Dev. 2008;22(4):416–29.

103. Chastney MR, Lawless C, Humphries JD, Warwood S, Jones MC, Knight D, et al. Topological features of integrin adhesion complexes revealed by multiplexed proximity biotinylation. J Cell Biol. 2020;219(8):34.

104. Fang WB, Brantley-Sieders DM, Hwang Y, Ham A-JL, Chen J. Identification and functional analysis of phosphorylated tyrosine residues within EphA2 receptor tyrosine kinase. Journal of Biological Chemistry. 2008;283(23):16017–26.

105. Finney AC, Scott ML, Reeves KA, Wang D, Alfaidi M, Schwartz JC, et al. EphA2 signaling within integrin adhesions regulates fibrillar adhesion elongation and fibronectin deposition. Matrix Biol. 2021;103:1–21.

Yildiz *et al. Epigenetics & Chromatin*   (2023) 16:42

Page 19 of 19

106. Walker-Daniels J, Coffman K, Azimi M, Rhim J, Bostwick D, Snyder P, et al. Overexpression of the EphA2 tyrosine kinase in prostate cancer. Prostate. 1999;41(4):275–80.

107. Ireton RC, Chen J. EphA2 receptor tyrosine kinase as a promising target for cancer therapeutics. Curr Cancer Drug Targets. 2005;5(3):149–57.

108. Wang TH, Chang JL, Ho JY, Wu HC, Chen TC. EphrinA5 suppresses colon cancer development by negatively regulating epidermal growth factor receptor stability. FEBS J. 2012;279(2):251–63.

109. Tandon M, Vemula SV, Mittal SK. Emerging strategies for EphA2 receptor targeting for cancer therapeutics. Expert Opin Ther Targets. 2011;15(1):31–51.

110. Miao H, Wang B, editors. EphA receptor signaling—complexity and emerging themes. Seminars in cell & developmental biology; 2012: Elsevier.

111. Miao H, Li D-Q, Mukherjee A, Guo H, Petty A, Cutter J, et al. EphA2 mediates ligand-dependent inhibition and ligand-independent promotion of cell migration and invasion via a reciprocal regulatory loop with Akt. Cancer Cell. 2009;16(1):9–20.

112. Liang L-Y, Patel O, Janes PW, Murphy JM, Lucet IS. Eph receptor signalling: from catalytic to non-catalytic functions. Oncogene. 2019;38(39):6567–84.

113. Peuckert C, Wacker E, Rapus J, Levitt P, Bolz J. Adaptive changes in gene expression patterns in the somatosensory cortex after deletion of ephrinA5. Mol Cell Neurosci. 2008;39(1):21–31.

114. Iida H, Honda M, Kawai H, Yamashita T, Shirota Y, Wang B, et al. Ephrin-A1 expression contributes to the malignant characteristics of α-fetoprotein producing hepatocellular carcinoma. Gut. 2005;54(6):843–51.

115. Schmid RS, Maness PF. L1 and NCAM adhesion molecules as signaling coreceptors in neuronal migration and process outgrowth. Curr Opin Neurobiol. 2008;18(3):245–50.

116. Maness PF, Schachner M. Neural recognition molecules of the immunoglobulin superfamily: signaling transducers of axon guidance and neuronal migration. Nat Neurosci. 2007;10(1):19–26.

117. Cui X-P, Wang C-X, Wang Z-Y, Li J, Tan Y-W, Gu S-T, Qin C-K. LncRNA TP73-AS1 sponges miR-141–3p to promote the migration and invasion of pancreatic cancer cells through the up-regulation of BDH2. Bioscience reports. 2019;39(3).

118. Roesler J, Srivatsan E, Moatamed F, Peters J, Livingston EH. Tumor suppressor activity of neural cell adhesion molecule in colon carcinoma. Am J Surg. 1997;174(3):251–7.

119. Katoh M, Katoh M. Identification and characterization of TPARM gene in silico. Int J Oncol. 2003;23(4):1213–7.

120. Chan AO, Lam S, Wong BC, Wong W, Yuen M, Yeung Y, et al. Promoter methylation of E-cadherin gene in gastric mucosa associated with Helicobacter pylori infection and in gastric cancer. Gut. 2003;52(4):502–6.

121. Chen M-W, Hua K-T, Kao H-J, Chi C-C, Wei L-H, Johansson G, et al. H3K9 histone methyltransferase G9a promotes lung cancer invasion and metastasis by silencing the cell adhesion molecule Ep-CAM. Can Res. 2010;70(20):7830–40.

122. Tai K, Shiah S, Shieh Y, Kao Y, Chi C, Huang E, et al. DNA methylation and histone modification regulate silencing of epithelial cell adhesion molecule for tumor invasion and progression. Oncogene. 2007;26(27):3989–97.

123. Mercer TR, Dinger ME, Mattick JS. Long non-coding RNAs: insights into functions. Nat Rev Genet. 2009;10(3):155–9.

124. Fang Y, Fullwood MJ. Roles, functions, and mechanisms of long non-coding RNAs in cancer. Genomics Proteomics Bioinformatics. 2016;14(1):42–54.

125. Li Y, Syed J, Sugiyama H. RNA-DNA triplex formation by long noncoding RNAs. Cell Chem Biol. 2016;23(11):1325–33.

126. Blank-Giwojna A, Postepska-Igielska A, Grummt I. lncRNA KHPS1 activates a poised enhancer by triplex-dependent recruitment of epigenomic regulators. Cell Rep. 2019;26(11):2904–15.

127. Miguel V, Lamas S, Espinosa-Diez C. Role of non-coding-RNAs in response to environmental stressors and consequences on human health. Redox Biol. 2020;37:101580. https://doi.org/10.1016/j.redox.2020.101580.

128. Ruffo P, De Amicis F, Giardina E, Conforti FL. Long-noncoding RNAs as epigenetic regulators in neurodegenerative diseases. Neural Regen Res. 2023;18(6):1243–8. https://doi.org/10.4103/1673-5374.358615.

129. Ma Y, Xue Y, Liu X, Qu C, Cai H, Wang P, et al. SNHG15 affects the growth of glioma microvascular endothelial cells by negatively regulating miR-153. Oncol Rep. 2017;38(5):3265–77.

130. Jin B, Jin H, Wu HB, Xu JJ, Li B. Long non-coding RNA SNHG15 promotes CDK14 expression via miR-486 to accelerate non-small cell lung cancer cells progression and metastasis. J Cell Physiol. 2018;233(9):7164–72.

131. Kong Q, Qiu M. Long noncoding RNA SNHG15 promotes human breast cancer proliferation, migration and invasion by sponging miR-211-3p. Biochem Biophys Res Commun. 2018;495(2):1594–600.

132. Svedružić ŽM. Dnmt1: Structure and function. Prog Mol Biol Transl Sci. 2011;101:221–54.

133. Svedruzic ZM. Mammalian cytosine DNA methyltransferase Dnmt1: enzymatic mechanism, novel mechanism-based inhibitors, and RNA-directed DNA methylation. Curr Med Chem. 2008;15(1):92–106.

134. Bestor TH. The DNA methyltransferases of mammals. Hum Mol Genet. 2000;9(16):2395–402.

135. Mohan KN, Chaillet JR. Cell and molecular biology of DNA methyltransferase 1. Int Rev Cell Mol Biol. 2013;306:1–42.

136. Pensold D, Zimmer-Bensch G. DNMT1-dependent regulation of cortical interneuron function and survival. Neural Regen Res. 2021;16(12):2405.

137. Merry CR, Forrest ME, Sabers JN, Beard L, Gao X-H, Hatzoglou M, et al. DNMT1-associated long non-coding RNAs regulate global gene expression and DNA methylation in colon cancer. Hum Mol Genet. 2015;24(21):6240–53.

138. Ma F, Lei Y-Y, Ding M-G, Luo L-H, Xie Y-C, Liu X-L. LncRNA NEAT1 interacted with DNMT1 to regulate malignant phenotype of cancer cell and cytotoxic T cell infiltration via epigenetic inhibition of p53, cGAS, and STING in lung cancer. Front Genet. 2020;11:250.

139. Huang W, Li H, Yu Q, Xiao W, Wang DO. LncRNA-mediated DNA methylation: an emerging mechanism in cancer and beyond. J Exp Clin Cancer Res. 2022;41(1):100.

140. Kunkler CN, Hulewicz JP, Hickman SC, Wang MC, McCown PJ, Brown JA. Stability of an RNA•DNA–DNA triple helix depends on base triplet composition and length of the RNA third strand. Nucleic Acids Res. 2019;47(14):7213–22. https://doi.org/10.1093/nar/gkz573.

141. Antonov IV, Mazurov E, Borodovsky M, Medvedeva YA. Prediction of lncRNAs and their interactions with nucleic acids: benchmarking bioinformatics tools. Brief Bioinform. 2019;20(2):551–64.

142. An integrated encyclopedia of DNA elements in the human genome. Nature. 2012;489(7414):57–74. https://doi.org/10.1038/nature11247.